

**Chemistry, Dynamics, and Radiation of Ozone Loss:
Airborne Measurements of OH, HO₂, NO₂, ClO, BrO, IO, ClONO₂, BrONO₂,
ClOOCl, and H₂O**

Final Summary of Research
NASA Langley Grant NAG1-01095
January 1, 2001–June 30, 2004

Submitted to
National Aeronautics and Space Administration
from
President and Fellows of Harvard College
c/o Office for Sponsored Programs
Holyoke Center, Suite 600
1350 Massachusetts Avenue
Cambridge, Massachusetts 02138

James G. Anderson, Principal Investigator
Division of Engineering and Applied Sciences and
Department of Chemistry and Chemical Biology
Harvard University
12 Oxford Street
Cambridge, MA 02138

May 17, 2005

A. Chemistry, Dynamics, and Radiation of Ozone Loss: Airborne Measurements of OH, HO₂, NO₂, ClO, BrO, IO, ClONO₂, BrONO₂, ClOOCl, and H₂O

B. Prof. James G. Anderson, Harvard University, 12 Oxford Street, Cambridge, MA 02138.
Phone: 617-495-5922; Fax: 617-495-4902; E-mail: anderson@huarp.harvard.edu;
<http://www.arp.harvard.edu/>

C. Abstract of Research Objectives:

This research addresses, through a combination of *in situ* and remote aircraft-borne instruments, the following scientific questions:

- Which mechanisms are responsible for the continuing erosion of ozone over midlatitudes of the Northern Hemisphere?
- Will the rapid loss of ozone over the Arctic in late winter continue to worsen over the next two decades? Are these large losses dynamically coupled to midlatitudes?
- Which mechanisms dictate the rate of exchange of material between the troposphere and stratosphere? How will these processes change in response to changes in climate?
- Will regional scale pollution episodes, that are emerging as predictable seasonal events, significantly affect the middle-to-upper troposphere chemical composition. If so, how will these changes alter the chemical composition of the middle world? What changes are predicted for the overworld?
- Why has the arctic stratosphere become colder in the late winter phase in recent years? Have increases in tropical upper troposphere temperatures increased the temperature gradient such as to change the trajectories of vertically propagating waves, thus reducing the effectiveness of the meridional circulation for transport of heat, momentum and ozone from the tropics to high latitudes?

D. Summary of Research:

The following report is submitted to detail progress over the period January 1, 2001, to June 30, 2004, under NASA Langley Grant NAG-1-0195. The report is organized around twenty sections that cover both scientific results and instrument development and calibration.

	Page
1. The photochemical coupling of ClOOCl and ClO in the Arctic polar vortex	2
2. Inorganic chlorine budget in the arctic winter	4
3. Evolution of chlorine in the arctic winter	5
4. Quantifying the rate of heterogeneous processing in the arctic polar vortex with <i>in situ</i> observations of OH	7
5. Direct <i>in situ</i> observations of the effects of the heterogeneous removal of HOCl in the arctic polar vortex	9
6. <i>In situ</i> observations of HO ₂ and OH obtained on the NASA ER-2 in the high ClO conditions of the 1999–2000 Arctic polar vortex	11
7. Comparing atmospheric [HO ₂]/[OH] to modeled [HO ₂]/[OH]: Identifying discrepancies with reaction rates	12
8. The effect of the ClOO + NO reaction on measurements of ClO	13
9. Analysis of NO ₂ exchange and the evolution of ClO/ClONO ₂ /NO ₂ during SOLVE	15
10. Chlorine-catalyzed polar ozone loss	17

11. Costa Rica progress report	17
12. Observations of supersaturation in the presence of cirrus in the subtropical upper troposphere: Results from CRYSTAL-FACE	27
13. Water vapor and total water instrumentation	29
14. The implications of stratospheric hydration events observed during a mini mission to Costa Rica in August 2001	35
15. Quantifying isentropic transport in the middleworld during CRYSTAL-FACE using tracer-tracer correlations and a simple mixing model	37
16. Observations of hydration in the upper troposphere by convective events: Case studies during CRYSTAL-FACE	39
17. Studying the evolution of cirrus clouds during CRYSTAL-FACE: A mixing model using tracer-tracer correlations	41
18. Equatorward isentropic transport of northern midlatitude stratospheric air observed over Florida during CRYSTAL FACE	44
19. Direct measurements of OH yields from gas-phase ozone-alkene reactions using an <i>in situ</i> LIF instrument	47
20. BrO measurements in the arctic winter stratosphere	47

1. The photochemical coupling of ClOOCl and ClO in the Arctic polar vortex

The first measurements of ClOOCl in the stratosphere have been acquired from a NASA ER-2 aircraft, deployed from Kiruna, Sweden (68°N, 21°E), during the joint SOLVE/THESEO mission of the winter of 1999/2000. Observations of the ratio $[\text{ClOOCl}]/[\text{ClO}]^2$ (estimated uncertainty of $\pm 25\%$, 1σ) are used, with a time-dependent photochemical model, to test the model representation of the ratios of kinetic parameters J/k^{Prod} and $k^{\text{Loss}}/k^{\text{Prod}}$ for day and nighttime observations, respectively (Stimpfle *et al.*, 2004). Here, k^{Prod} and k^{Loss} are the rate constants for ClOOCl production and loss, respectively, and J is the photolysis rate of ClOOCl.

In this analysis values for k^{Prod} are taken from: the 2000 JPL Evaluation (Sander *et al.*, 2000) (k^{JPL00}); the recent laboratory work of Bloss *et al.* (2001) (k^{Bloss}); the earlier work of Trolrier *et al.* (1990) (k^{Trolrier}); and the 2002 JPL Evaluation (Sander *et al.*, 2002) (k^{JPL02}). These four values span the range of variation of different measurements of k^{Prod} . Bloss *et al.* (2001) report k^{Prod} to be ~ 30 to 20% faster than k^{JPL00} over the temperature range characteristic of this data set, $190 < T < 200$ K, respectively. The value given by k^{JPL02} is the most rapid over this T range, ~ 35 to 25% faster than k^{JPL00} , respectively. The earlier k^{Trolrier} value is ~ 10 to 15% slower than k^{JPL00} over this T range, respectively. Values for J^{ClOOCl} are derived from cross sections from four sources: Huder and DeMore (1995) (J^{Huder}); the JPL02 recommendation (J^{JPL02}), which is unchanged from JPL00; Burkholder *et al.* (1990), extrapolated to 450 nm ($J^{\text{Burkholder}}$); and a speculative J value based upon an assumption of additional photolysis in the near IR tail of the absorption curve (J^{NearIR}).

The daytime analysis is summarized by the plot of β versus SZA where,

$$\beta = \left(\frac{[\text{ClOOCl}]}{[\text{ClO}]^2} \right)^{\text{Obs}} \bigg/ \left(\frac{[\text{ClOOCl}]}{[\text{ClO}]^2} \right)^{\text{Model}}$$

β is calculated for various model runs, for all of the simultaneous, daytime observations (Obs) of ClO and ClOOCl obtained during SOLVE. β is regressed against SZA to examine the accuracy of the J value as a function of SZA. The analysis uses a time-dependent, 24-hour, photochemical

model (Salawitch *et al.*, 1993). Kinetic parameters used in the model are from JPL 2002 (Sander *et al.*, 2002) except as otherwise specified. The J value is calculated from the ClOOC1 absorption cross sections, using a radiative transfer model (Salawitch *et al.*, 1994) constrained by maps of ozone reconstructed using measurements from the Polar Ozone Aerosol Measurement (POAM) III satellite instrument (Randall *et al.*, 2002).

When β equals unity there is agreement between the observations and the model. The interpretation of the results of Figure 1 is somewhat complicated by the fact that we can test only the ratio of J over k^{Prod} , not individual values of either J or k^{Prod} . We have therefore plotted every permutation of the four choices of J and k^{Prod} in panels b, c, d and e of Figure 1.

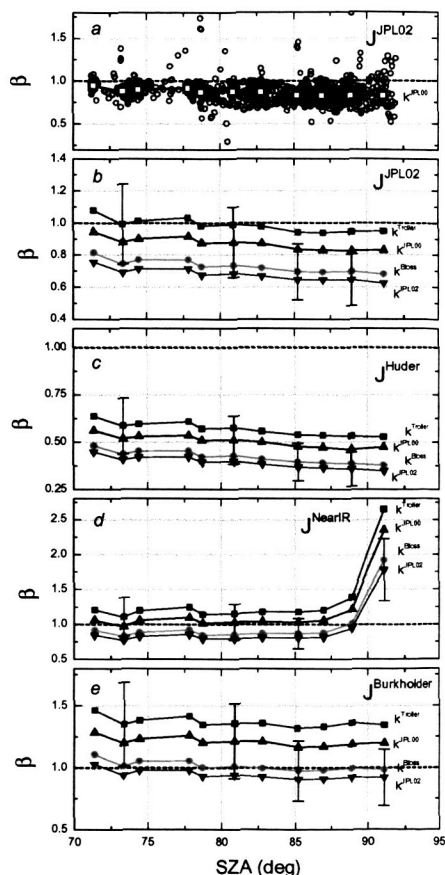


Figure 1: Daytime analysis of all flights, β (unitless) vs SZA (deg). Data selected for SZA < 92° and $M < 3.0 \times 10^{18}$ molec cm⁻³. (a) Unaveraged and averaged data for the standard case, k^{JPL00} and J^{JPL02} . Averages are calculated for 2° width bins from 70 to 92° SZA. (b) Average values for J^{JPL02} and four different values for k^{Prod} as indicated. (c) As above but for J^{Huder} . (d) As above but for J^{NearIR} . (e) As above but for $J^{\text{Burkholder}}$. Error bars depict $\pm 25\%$ error attributable to the observations.

The observations are in good agreement with J^{JPL02} , if the true value of k^{Prod} is given by k^{JPL00} or k^{Trier} . The more rapid values of k^{Prod} given by k^{Bloss} and k^{JPL02} are consistent with the observations only if J is increased by a significant amount. This is accomplished if J is calculated with the larger ClOOC1 cross sections measured by Burkholder *et al.* (1990), $J^{\text{Burkholder}}$. The J values of J^{Huder} are too small, by factors of ~ 1.6 to 2.5 for all values of k^{Prod} , based on the observations. Both J^{Huder} and J^{NearIR} are effectively ruled out by the observations of ClO and ClOOC1.

Increasing both J and k relative to JPL00 recommendations will lead to substantial increases in the calculated rate of ozone destruction by the ClO dimer cycle, because chlorine is cycled more quickly through the various steps of the cycle. A separate analysis of nighttime results suggest that, for $190 < T < 200$ K, the values for K^{Eq} (the equilibrium constant, equal to

the ratio of $k^{\text{Prod}}/k^{\text{Loss}}$ of Cox and Hayman (1988) and Avallone and Toohey (2001) are in best agreement with the observations.

2. Inorganic chlorine budget in the arctic winter

Given the clear link between active chlorine abundance and ozone levels, it is critical that all of the inorganic chlorine in the stratosphere is quantitatively accounted for and that the chlorine budget is understood. Simultaneous measurements of ClO , ClOOCl , ClONO_2 , HCl , and Cl_y during the SOLVE (SAGE III Ozone Loss and Validation Experiment) mission enable the inorganic chlorine budget to be evaluated in the polar vortex for the first time. The analysis of interest is to test whether the sum of ClO_x , ClONO_2 , and HCl is equivalent to total inorganic chlorine, Cl_y .

The inorganic chlorine budget agreement inside the vortex throughout the entire SOLVE mission is summarized in Figure 2, where $(\text{ClO}_x + \text{ClONO}_2 + \text{HCl})/\text{Cl}_y$ at cruise altitude is plotted as a function of Julian Date in 2000. The vertical points indicate the range of budget agreement observed for each ER-2 flight day, and the open circles are the mean values. The first flight of the second deployment, 0226, is not shown due to the absence of HCl data. The 0123 flight is shown but includes calculated ClOOCl .

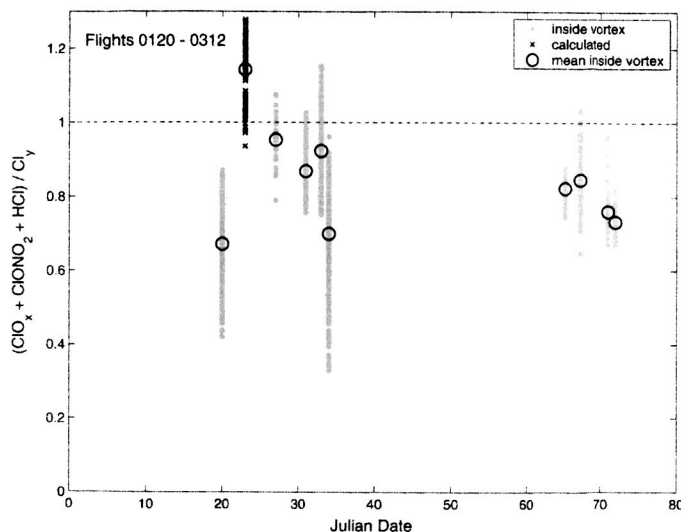


Figure 2: Inorganic chlorine budget agreement inside the vortex throughout the course of the SOLVE mission, 0120 - 0312. The vertical points indicate the range of agreement observed at cruise altitude on Julian Dates that the ER-2 flew in 2000, and the open circles represent the mean values observed. The ClOOCl data included in the 0123 flight are calculated. The dotted line at 1.0 represents complete budget agreement.

Analysis of the first deployment data in Figure 2 reveals that the flights of 0120 and 0123 are outliers in budget agreement. That 0120 is so low lends support to the notion that there is a missing chlorine species not being measured, likely Cl_2 . The 0123 flight is considerably higher than the others, with a mean budget agreement of 1.14 and values as high as 1.27, suggesting the calculation of ClOOCl using the PSS approximation may not be accurate for this flight. The flights of 0127, 0131, and 0202 agree well with each other and represent good overall budget agreement, as $(\text{ClO}_x + \text{ClONO}_2 + \text{HCl})/\text{Cl}_y = 0.91$ for the average of the three. The final flight of the first SOLVE ER-2 deployment, 0203, is significantly lower than the previous four. This was a nighttime stacked flight over Kiruna; thus, the budget disagreement may indicate a density-dependent error in one or more of the measurements.

Comparison of the four flights of the second deployment with the three 'representative' flights (0127, 0131, and 0202) of the first deployment reveals that the budget agreement is worse for all of the later flights. The mean budget agreement is 0.79, and there is generally a downward trend, indicating that the budget became more in error as the second deployment progressed. This suggests that there may be a measurement error in one of the reservoir chlorine species, as active

chlorine is becoming a smaller fraction of the budget and recovery is taking place. It is also possible that there is an error in the ACATS Cl_y measurement or that there is a missing chlorine species; however, these are less likely given that measured Cl_y yields good budget results in the first deployment, and a missing chlorine species would need to be present at a mixing ratio > 500 ppt.

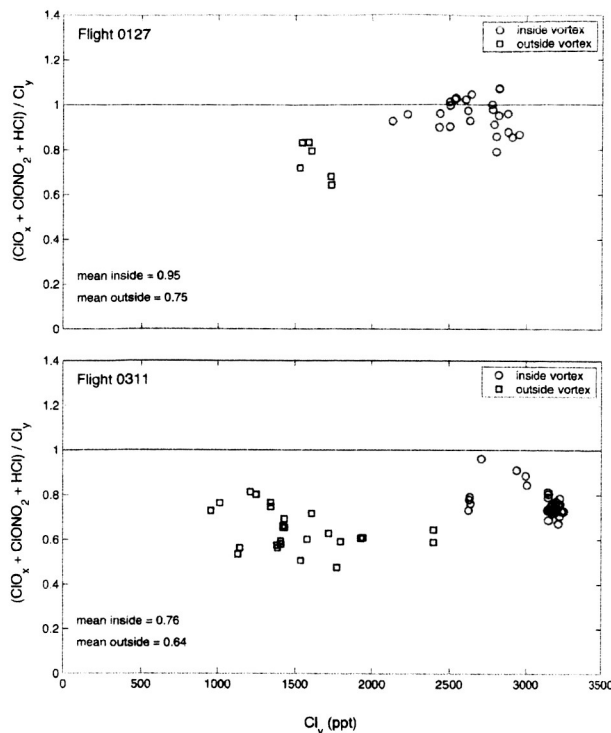


Figure 3: Inorganic chlorine budget agreement as a function of Cl_y for the two extratropical SOLVE flights: 0127 (Top) and 0311 (Bottom). Data for both inside and outside the vortex are shown. The dotted lines at 1.0 represent complete budget agreement.

One way to eliminate ClO_x as a possible source of the budget discrepancy and to evaluate measured ClONO_2 and HCl is to examine the extratropical data from SOLVE. Outside the vortex, $\text{ClONO}_2 + \text{HCl}$ typically comprises 90–95% of Cl_y . The only extratropical HCl data available for the SOLVE mission are from segments of the 0127 and 0311 flights. The budget agreement as a function of Cl_y for these two flights is shown in Figure 3. In both cases, the budget agreement is significantly worse outside than inside the vortex, and more generally, good budget agreement is only attained when ClO_x comprises the vast majority of Cl_y . This implies that there is a measurement error in ClONO_2 or HCl . Given the magnitude of the extratropical budget discrepancy, it is likely that HCl is at least partly the cause, as ClONO_2 alone would need to be in error by nearly a factor of two to establish agreement on 0127 and almost a factor of three on 0311. Calculations of ClONO_2 from a photochemical steady-state expression using measured ClO and NO_2 serve to further validate the ClONO_2 measurements (see “Analysis of NO_2 exchange and the evolution of $\text{ClO}/\text{ClONO}_2/\text{NO}_2$ during SOLVE”). This suggests that ClONO_2 is not the source of the budget discrepancy. Thus, measured HCl is most likely the primary source of the observed budget discrepancy during SOLVE, as was the case in previous missions (Bonne *et al.*, 2000).

3. Evolution of chlorine in the arctic winter

Acquisition of the first *in situ* stratospheric ClOOCl measurements during the SOLVE (SAGE III Ozone Loss and Validation Experiment) mission, along with concurrent measurements of ClO , allow the evolution of active chlorine, ClO_x ($= \text{ClO} + 2 \times \text{ClOOCl}$), to be monitored throughout the polar winter for the first time. In conjunction with values of total

inorganic chlorine, Cl_y , inferred from measurements of organic chlorine source gases by the ACATS instrument, the partitioning of chlorine into its active form can be determined.

The results from all of the ER-2 SOLVE flights are summarized in Figure 4. The fraction of chlorine in its active form, ClO_x/Cl_y , at cruise altitude is plotted as a function of Julian Date in 2000, effectively allowing the evolution of chlorine activation to be tracked throughout the Arctic winter. While plotting all of the ClO_x/Cl_y data from each flight at a single point on the abscissa allows a clear determination of the range of ClO_x/Cl_y observed, the number of points contributing to each value within that range is obscured. For that reason, the mean fraction of active chlorine for each flight in the vortex is indicated with an open circle.

Measurements for 9 of the 11 intravortex SOLVE flights originating in Kiruna are shown here. The flight of 0203 is not included because it was a stacked flight, in which the altitude sampled is distinct from the other flights. Measurements of ClOOCl from 0123 are also not included in this figure due to an instrument problem on that flight. However, ClOOCl is determined from measured ClO using the photochemical steady-state approximation adjusted with a correction factor consistent with the other flights. The results for 0123 thus produced are indicated as 'calculated' on the plot. Also shown in Figure 4 are ClO_x/Cl_y measurements from outside the vortex. These include two flights from Kiruna which sampled extravortex air (0127 and 0311), the transits to (0114) and from Kiruna (0316), and three flights from the United States in early January prior to SOLVE.

ClO_x/Cl_y is less than 0.10 for all flights outside the vortex. Inside the vortex, ClO_x/Cl_y is highly elevated, typically reaching a maximum around 0.85 with a mean of approximately 0.78 in the first ER-2 deployment (second phase of SOLVE). Two notable exceptions to this are the flights of 0120, which is considerably less than the others, and 0123, which is substantially higher, effectively indicating full chlorine activation. Analysis of the back trajectories for 0120 reveals that the air sampled in this flight had not been exposed to sunlight for the previous 10 days; it therefore seems likely that much of the inorganic chlorine was still in the form of Cl_2 , the product of heterogeneous reactions on PSCs. While ClOOCl for 0123 was calculated, it was done so with an expression that precisely reproduces ClOOCl as measured for all the other flights, so there is no *a priori* reason to discount these ClO_x/Cl_y data. This was a unique flight in that it took place at sunrise, the first ER-2 flight following the return of daylight to the polar vortex. It is possible that ClO_x/Cl_y peaked under these conditions as the photolabile products of heterogeneous reactions were rapidly converted into ClO_x in sunlight. In the absence of actual ClOOCl measurements, it cannot be discerned for certain if this is a real effect.

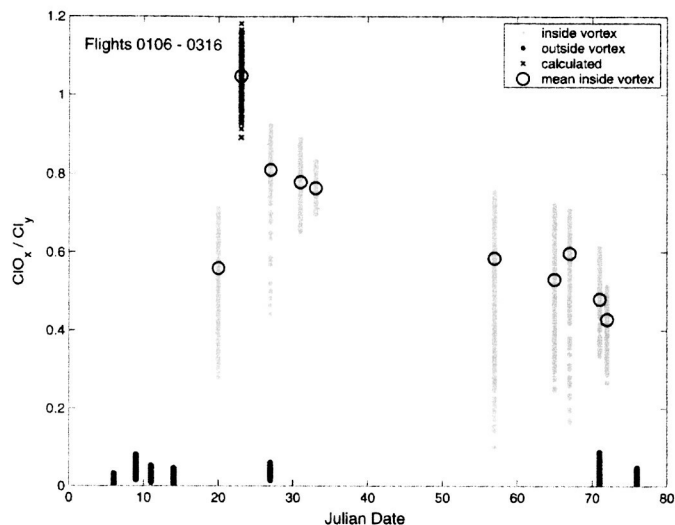


Figure 4: Partitioning of inorganic chlorine into its active form over the course of the entire SOLVE mission and three flights prior to SOLVE, 0106 - 0316. The vertical points indicate the range of ClO_x/Cl_y observed at cruise altitude on Julian Dates that the ER-2 flew in 2000, and the open circles represent the mean values observed for the flights inside the Arctic vortex. ClO_x/Cl_y was calculated for 0123 and is not shown for 0203.

ClO_x/Cl_y inside the vortex during the second SOLVE ER-2 deployment (third mission phase) is still highly elevated but lower than during the first deployment. In addition, the fraction of active chlorine generally decreases throughout the flights of the second deployment. The mean values inside the vortex range from 0.58 on 0226 to 0.43 on 0312. These decreasing levels of intravortex ClO_x are indicative of recovery, the replacement of active chlorine with reservoir forms.

4. Quantifying the rate of heterogeneous processing in the arctic polar vortex with *in situ* observations of OH

We present simultaneous *in situ* observations of OH, HO_2 , ClONO_2 , HCl, and particle surface area inside a polar stratospheric cloud undergoing rapid heterogeneous processing. A steady-state analysis constrained by *in situ* observations is used to show that calculations of HO_x during a processing event are extremely sensitive to the assumptions regarding aerosol composition and reactivity. This analysis shows that large perturbations in the abundance of OH and HO_2 are consistent with the heterogeneous production of HOCl via



and removal via



in a polar stratospheric cloud.

Due to the short lifetime of OH, the production of OH from heterogeneous reactions must be instantaneous. That is, the processing via *R1* and *R2* occur *during* the ER-2 encounter. This is the first time that the products of heterogeneous reactions have been observed *in situ* during a heterogeneous event. Since *R1* and *R2* occur at the time of the encounter, we have an unprecedented opportunity to compare the *instantaneous* rates of heterogeneous reactions with *in situ* observations. The agreement between the measured and calculated concentrations of OH suggests that accounting for the presence of both STS and NAT and the modifications for HNO_3 content in STS aerosols and low HCl coverage on NAT are required.

If the cloud is composed of super-cooled ternary solution (STS) aerosols and solid nitric acid trihydrate (NAT) particles, comparison with observations of OH show that modifications to surface reactivity to account for high HNO_3 content in STS aerosols and low HCl coverage on NAT particles are appropriate. These results indicate that with the low HCl levels in this encounter and in a processed polar vortex in general, reactions on STS aerosols dominate the total heterogeneous processing rate. As a consequence, the formation of NAT does not lead to significantly faster reprocessing rates when HCl concentrations are low and STS aerosols are present. Model calculations that include these modifications to uptake coefficients for STS and NAT will lead to significantly slower reprocessing and faster recovery rates of chlorine in the springtime Arctic polar vortex.

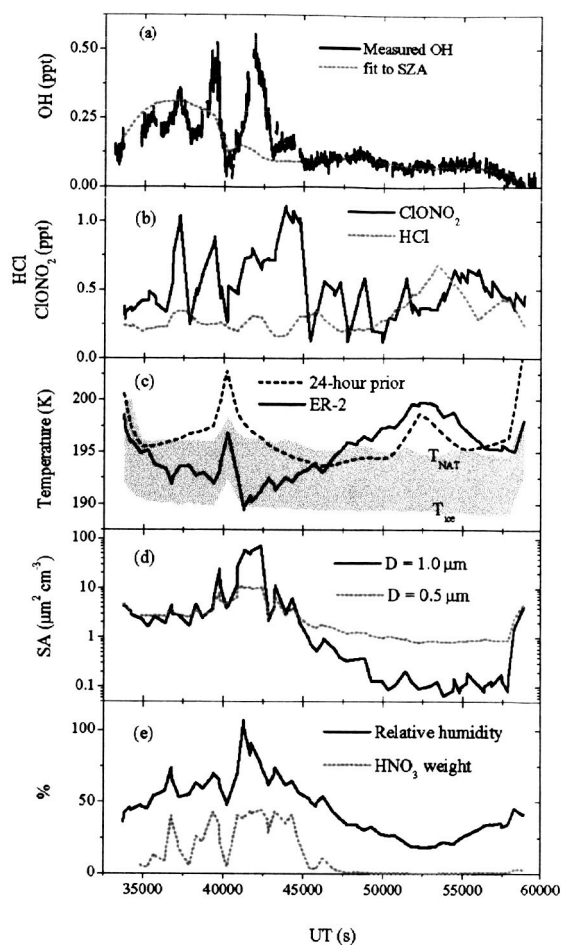


Figure 5: (a) Observations from the flight of March 5, 2000 are plotted *versus* universal time (UT). This daytime flight occurred within the polar vortex. The flight began with an eastbound leg that intercepted the cold pool, followed by north, west, and southbound legs. In (a) the measured OH is compared to a fit of OH *versus* SZA. (b) ClONO_2 and HCl. (c) Temperatures measured during the flight by the MMS instrument and the temperature 24 hours prior to the flight are shown. The shaded region is bounded by the threshold temperatures for NAT and H_2O ice formation. (d) Particle surface areas derived from the size distributions measured by the MASP instrument. All particles with $D < 0.7 \mu\text{m}$ are included in the $0.5 \mu\text{m}$ mode, and particles with $D > 0.7 \mu\text{m}$ are included in the $1.0 \mu\text{m}$ mode. (e) Calculated relative humidity and HNO_3 weight percent in particles assuming $\text{HNO}_3/\text{H}_2\text{SO}_4/\text{H}_2\text{O}$ solutions.

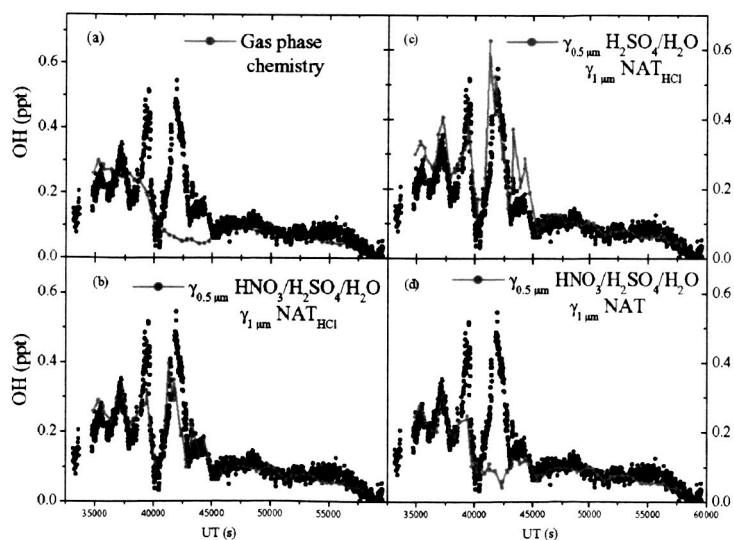


Figure 6: shows a comparison of the OH observed on the flight of March 5 with the concentrations of OH calculated from a model using different rates for R_1 and R_2 : a) Gas phase only, b) heterogeneous rates assuming $\text{HNO}_3/\text{H}_2\text{SO}_4/\text{H}_2\text{O}$ for the $0.5 \mu\text{m}$ mode and NAT with a strong HCl dependence for the $1 \mu\text{m}$ aerosol mode, c) JPL-00 recommendation for liquid $\text{H}_2\text{SO}_4/\text{H}_2\text{O}$ for the $0.5 \mu\text{m}$ mode and NAT with HCl dependence for the $1 \mu\text{m}$ aerosol mode, and d) $\text{HNO}_3/\text{H}_2\text{SO}_4/\text{H}_2\text{O}$ for the $0.5 \mu\text{m}$ mode and NAT with no HCl dependence for the $1 \mu\text{m}$ aerosol mode.

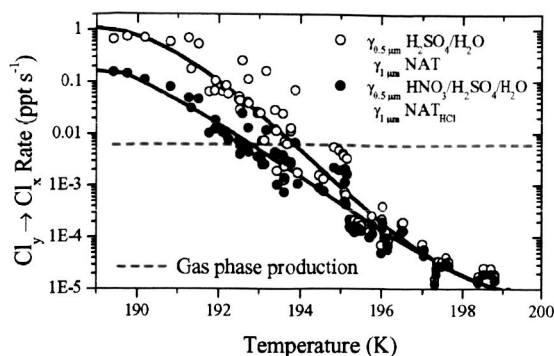


Figure 7: The instantaneous removal rate of ClONO_2 by (1) and (2) calculated using the reactivities that include modifications for HNO_3 content in liquid aerosols and HCl coverage on NAT compared to the rate using the unmodified gammas. Also shown is the average instantaneous gas phase production rate of ClONO_2 in the PSC (the rates of $\text{HNO}_3 + h\nu$ and $\text{OH} + \text{HNO}_3$ determined from observation). Model calculations that do not include modifications to account for HNO_3 content in liquid aerosols and HCl coverage on NAT overpredict the conversion rate of $\text{Cl}_y \rightarrow \text{Cl}_x$ by ~ 10 .

5. Direct *in situ* observations of the effects of the heterogeneous removal of HOCl in the arctic polar vortex

SOLVE results show that *in situ* measurements of OH and HO_2 (HO_x) can provide a sensitive diagnostic for the occurrence of heterogeneous chemistry within the Arctic polar vortex. Measurements of OH from the flight of January 23, 2000, provide spectacular observational evidence of heterogeneous processing via the reaction $\text{HOCl} + \text{HCl} + \text{aerosol} \rightarrow \text{H}_2\text{O} + \text{Cl}_2$. OH concentrations during the sunrise portion of this flight are nearly zero. They are a small fraction of the levels expected from gas phase processes and show a marked deviation from the canonical $\text{OH}:\text{SZA}$ parameterization, Figure 8. In fact, these are the lowest concentrations of HO_x encountered in the lower stratosphere at these solar zenith angles. Results of an analysis of simultaneous *in situ* observations of a number of stratospheric trace species including OH and HO_2 , and meteorological parameters acquired aboard the NASA ER-2, show that the absence of HO_x in this air mass is a consequence of the near complete heterogeneous removal of HOCl the previous night. Because of the tight coupling of HOCl to HO_x , via the fast gas phase reactions $\text{HO}_2 + \text{ClO} \rightarrow \text{HOCl} + \text{O}_2$, and $\text{HOCl} + h\nu \rightarrow \text{OH} + \text{Cl}$, heterogeneous loss of HOCl prior to sunrise will suppress OH for several hours. The January 23 sunrise observations of OH exhibit this dramatic signature of heterogeneous processing.

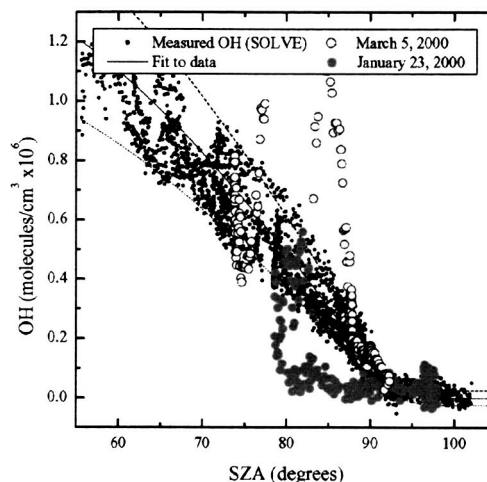


Figure 8: Measured OH is plotted as a function of SZA. OH observations from the entire SOLVE data set are plotted in black. The solid black line is a fit to the OH data, and is generated solely as a function of SZA. The anomalous flights of January 23, 2000, and March 5, 2000 (Hanisco *et al.*, 2002) are highlighted in green and blue respectively.

The direct reaction of HOCl with HCl , can prolong the duration of chlorine activation within the polar vortex into late winter/early spring, and lead to enhanced ozone loss. This reaction provides a mechanism for continuing the rapid conversion of HCl to ClO_x in the absence of ClONO_2 . The reaction sequence diagrammed below, beginning with the chlorine atom initiated oxidation of methane, highlights the role of (3) in preserving active chlorine, Figure 9. The sequence can result in either recovery via the net conversion of ClO_x to HCl in the absence

of heterogeneous chemistry (P1), or to a continuation of ozone loss in the presence of (3), (P2). The figure also captures the close coupling between HOCl and the HO_x family.

We use *in situ* data in combination with a time-dependent integrating photochemical model to explore how gas phase and heterogeneous processes, in particular, affect HO_x concentrations. Model results without inclusion of heterogeneous chemistry show remarkable agreement with measurements of OH in a chemically unperturbed airmass encountered on the flight of January 23, 2000. Furthermore, they are consistent with the OH concentrations expected from standard instantaneous steady-state chemistry, where $[OH] \approx \text{Production}_{HO_x} / \text{Loss}_{HO_x}$, as well as the OH concentrations expected from the SZA fit. This agreement validates our understanding of gas phase HO_x chemistry.

Model results with the inclusion of reaction (3), when initialized with 100 pptv of HOCl, show that heterogeneous chemistry occurring along the flight track is not fast enough to reproduce the observed OH suppression. Gas phase chemistry dominates during the sunlit conditions of the flight. Back-trajectory data, however, show that in its recent history the airmass has been subject to roughly 36 hours of sustained darkness, and simultaneous cooling. Initializing the model with HOCl₀ = 0 pptv, in order to simulate a nighttime loss of HOCl, yields results consistent with OH observations.

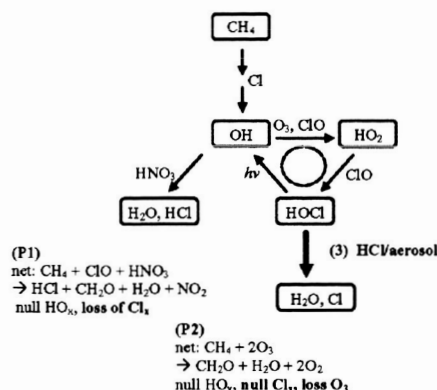


Figure 9: This figure captures the tight coupling between the hydroxyl radicals OH and HO₂ (HO_x) and one subset of the chlorine activation and recovery sequences. Chlorine recovery occurs via the chlorine atom initiated oxidation of methane. (P1) completes the chlorine and nitrogen recovery sequence through the gas phase loss of OH. (P2) perpetuates chlorine activation via the heterogeneous removal of HOCl.

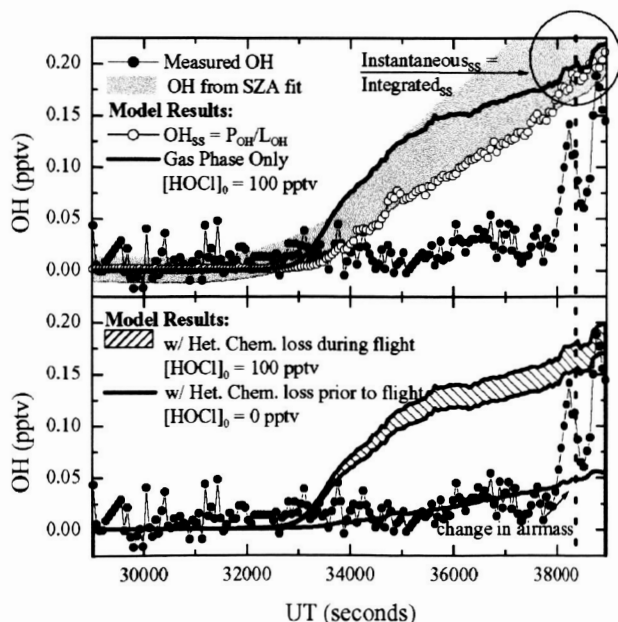


Figure 10: The results of a step-wise integrating model of OH are plotted as a function of time for the flight of January 23, 2000. The model, initialized with 100 pptv HOCl, uses production and loss rates calculated from measurements along the flight trajectory to simulate the evolution of OH in a homogenous airmass at sunrise. The top panel shows the agreement between integrated OH (blue line), instantaneous steady-state OH (open circles), and OH determined solely as a function of solar zenith angle (shaded area). Observed OH is plotted for comparison (black circles). The bottom panel shows the results of the model run with the inclusion of reaction HOCl + HCl. The range in the heterogeneous data is a result of different reaction rate parameters. Also shown, are the results of the integrating model initialized with HOCl₀ = 0, which simulates a nighttime loss of HOCl. This is the only way to achieve suppressed OH at sunrise.

In general, the time-dependent results show the sensitivity of OH at sunrise to the initial/nighttime value of HOCl. Deviations from the instantaneous steady-state values are attributed to the rapid repartitioning of HO_x species. When HOCl₀ = 100 pptv, OH is enhanced at sunrise due to HOCl photolysis. After the first hour of solar exposure, however, the integrated and instantaneous model results converge. By contrast, when HOCl₀ = 0 pptv, a condition which requires the complete heterogeneous removal of HOCl by (3) prior to sunrise, OH concentrations are suppressed for many hours. The latter scenario best describes the OH observations.

6. *In situ* observations of HO₂ and OH obtained on the NASA ER-2 in the high ClO conditions of the 1999–2000 Arctic polar vortex

Extensive observations of OH and HO₂ obtained aboard the NASA ER-2 inside the Arctic polar vortex during the SAGE III Ozone loss and Validation Experiment (SOLVE) provide the opportunity to identify and test interferences during the measurement of HO₂ in the presence of high concentrations of ClO. Measurements of HO₂, OH, ClO, and O₃ are used with rate constants derived from laboratory measurements to (1) test the consistency of the reactions that control HO₂/OH; (2) calculate the abundance of HOCl; and (3) determine the rate of the removal of O₃ through the reaction sequences:

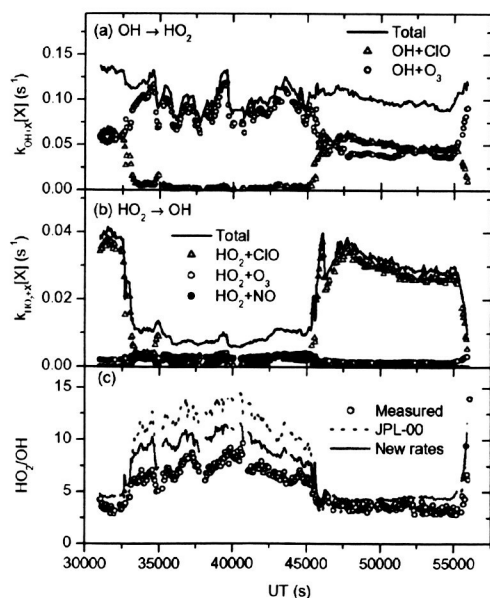
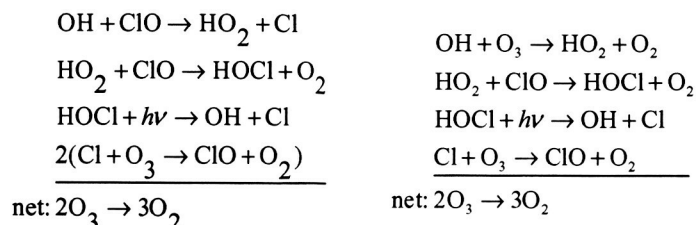


Figure 11: First-order rates for the conversion of (a) OH → HO₂ and (b) HO₂ → OH by reaction with X = O₃, ClO, and NO for the vortex edge crossing flight of March 11, 2000. The flight begins and ends inside the vortex with the crossings at UT = 32500 and 45000 s. The rates for small terms, e.g. OH + CH₄ and HO₂ + BrO, are not shown, but these rates are included in the total. (c) Measured and calculated HO₂/OH using JPL-00 rates and the recently determined rates.

Inside the vortex, the calculated HO₂/OH under-predicts the observed HO₂/OH by 7% with the JPL-00 rate constants and over-predicts the observations by 23% when recent laboratory rates are used. Thus (12) is consistent with a rate constant for HO₂ + ClO within $-7^{+45}_{-32}\%$ of the JPL-00 recommendation ($k_{\text{HO}_2+\text{ClO}} = 1.7 \pm 0.7 \times 10^{-11} \text{ molecules}^{-1} \text{ cm}^3 \text{ s}^{-1}$) and $23^{+45}_{-32}\%$ of the mean of the recent laboratory measurements ($k_{\text{HO}_2+\text{ClO}} = 1.1^{+0.8}_{-0.1} \times 10^{-11} \text{ molecules}^{-1} \text{ cm}^3 \text{ s}^{-1}$).

Measurements of HO_2 and ClO are also used to calculate ozone loss rates and concentrations of HOCl with uncertainties determined from the analysis of HO_2/OH . The concentration of HOCl is determined using a steady state relation and observations of HO_2 , ClO , and column O_3 . The calculated concentration of HOCl is 52^{+50}_{-28} pptv, or $0.07 \times \text{ClO}$ on average in the vortex.

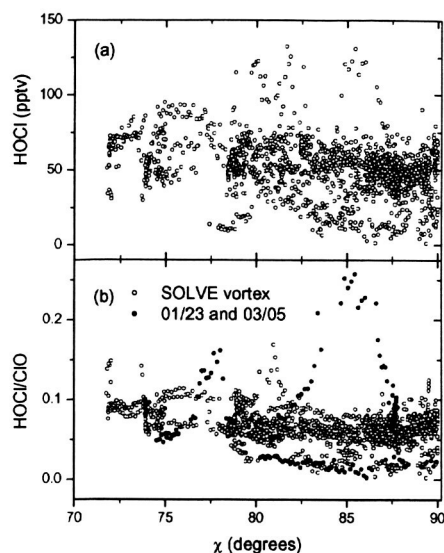


Figure 12: (a) The calculated HOCl mixing ratio and (b) the ratio HOCl/ClO inside the Arctic vortex are shown versus solar zenith angle. In (b) the data that are obtained during or immediately after heterogeneous processing (January 23 and March 5, 2000) are highlighted. The data are restricted to $M < 3 \times 10^{18} \text{ molecules cm}^{-3}$, $\chi < 90^\circ$ and $\text{ClO} > 200 \text{ pptv}$.

The ozone loss rate from the $\text{HO}_2 + \text{ClO}$ cycles is determined from the 24 hour average concentration of HO_2 and ClO using the rate limiting step in the catalytic cycles. The ozone loss rate from the two cycles controlled by $\text{HO}_2 + \text{ClO}$ is $\sim 1.5^{+1.2}_{-0.5} \text{ ppbv day}^{-1}$ in early March.

7. Comparing atmospheric $[\text{HO}_2]/[\text{OH}]$ to modeled $[\text{HO}_2]/[\text{OH}]$: Identifying discrepancies with reaction rates

Reactions that inter-convert OH and HO_2 are directly involved in the catalytic removal of O_3 in the lower stratosphere and in the catalytic production of O_3 in the upper troposphere. The agreement between the measured and modeled $[\text{HO}_2]/[\text{OH}]$ tests our current understanding of this important chemistry. Recent changes to the recommended rate constants for $\text{OH} + \text{O}_3$ and $\text{HO}_2 + \text{O}_3$ call into question how accurately the chemistry of the stratosphere is understood. In this analysis we use the large data set of in situ observations of NO , O_3 , CO , ClO , BrO , and CH_4 to investigate the discrepancies between measured and calculated HO_2/OH .

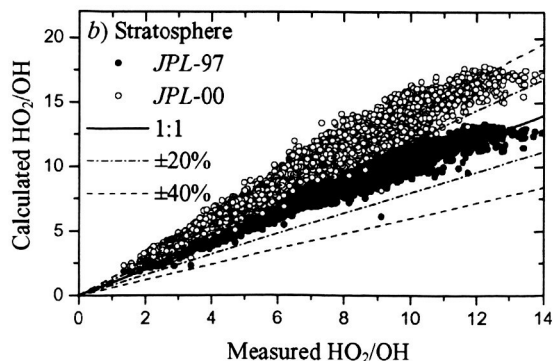


Figure 13: Measured $[\text{HO}_2]/[\text{OH}]$ versus the calculated ratio using *JPL-97* and *JPL-00* for stratospheric (ASHOE/MAESA and POLARIS) data averaged at 1 min. intervals. Data are restricted with the criteria $\text{SZA} < 80^\circ$ and air number density $< 2.5 \times 10^{18} \text{ molecules cm}^{-3}$. The dashed lines show the 20% uncertainty of the $[\text{HO}_2]/[\text{OH}]$ measurement. The 40% error bars are shown for reference.

$[\text{HO}_2]/[\text{OH}]$ calculated with the new recommendations is 48% higher than the observations throughout the lower stratosphere, exceeding the uncertainty limits of the

observations (20%), shown in Figure 13. Regressions of the error are consistent with errors in the $\text{OH} + \text{O}_3$ and $\text{HO}_2 + \text{O}_3$ rate constants or with errors in the observations that correlate with O_3 .

8. The effect of the $\text{ClOO} + \text{NO}$ reaction on measurements of ClO

Fractional yields for ClO to Cl conversion are required for analysis of flight data to derive ClO measurements (Anderson *et al.*, 1980; Brune *et al.*, 1989; Stimpfle *et al.*, 2004). Yields are calculated with a model based upon flight conditions of T , P , flow velocity, $[\text{O}_3]$ and $[\text{NO}]$. The kinetics of the conversion of ClO to Cl by reaction with NO had been thought to be adequately described by the following reaction sequence:



Since (2) is a Cl loss process, excessively high concentrations of NO will irreversibly remove Cl atoms to form ClNO . Thus NO addition in flight is varied to continually check that the yield is optimized.

However, an examination of the instrumental flight data from SOLVE has shown that Cl atoms are lost in excess NO more rapidly than the reaction sequence above can allow, especially as T decreases. Thus the presence of another non-negligible Cl removal process is indicated that will necessarily lower the calculated yield of Cl atoms and thus raise measured values of ClO . A plausible mechanism is the reaction of ClOO with NO through the following reaction sequence (Wilmouth, 2002):



The relative importance of this mechanism is expected to be extremely T -dependent due to the thermal instability of ClOO . Laboratory measurements of the rate constant for ClOO production (Nicholas and Norrish, 1968; Nicovich *et al.*, 1991; Baer *et al.*, 1991) and the equilibrium constant for ClOO formation (Nicovich *et al.*, 1991; Baer *et al.*, 1991; Mauldin *et al.*, 1992; Avallone, 1993) have been reported and evaluated (Sander *et al.*, 2002). There is one published, relative measurement of the rate constant of (7) at room temperature (Wongdontri-Stupor *et al.*, 1978). Our understanding of reaction (7) would benefit from further laboratory work, particularly at cold temperatures.

Evidence for the importance of (7) emerges from an examination of the observed Cl fluorescence signal as a function of NO concentration and temperature. The SOLVE flight of 3-5-2000 is particularly revealing, since the ambient T varied from 192 K to 200 K during an uninterrupted section of cruise flight. The analysis is based on a comparison between the observed ratios of the Cl signal at the lowest NO flow relative to the three larger NO flows (hereafter referred to as the 'yield ratio') and model calculations assuming various scenarios of reaction mechanisms and rate constants. The conclusions are summarized in Figure 14.

The observed yield ratios shown as the symbols are the average values from two regions of the 0305 flight where the temperatures in the sample duct were 212 and 220 K, corresponding to ambient temperatures of 192 and 200 K, respectively. Since four NO flows are used there are three values of the yield ratio at each T. The only parameters that can cause changes in the observed yield ratios are (a) a change in the actual NO flows used, (b) a change in the flow velocity through the instrument affecting reaction times and NO mixing ratio, and (c) a change in the yield because of an extreme temperature-dependent reaction mechanism. Possibilities (a) and (b) can be ruled out because the NO flow rates and the velocity measurements show no changes correlated with the observed changes in the yield ratios.

The most plausible explanation for the observed yield ratios is (c), an extreme temperature-dependent reaction. The red and blue lines of Figure 14a represent model calculations of the yield ratio for the conditions representative of the duct for this flight segment, $P = 67$ torr, velocity = 9 m/s, and $O_3 = 1.6$ ppmv, and where the rate constant for (7) is varied, $k^{ClOO+NO} = 3 \times 10^{-11}$ and 0 ($\text{cm}^3 \text{ molec}^{-1} \text{ s}^{-1}$), respectively. Clearly, the mechanism without the $ClOO + NO$ reaction does not match the relative yield at any temperature very well, but more importantly, cannot impart a temperature dependence to the observed yield ratios for the over-titrated points, which here are the points at yield ratios < 0.5 . The mechanism using $k^{ClOO+NO} = 3 \times 10^{-11}$ imparts a T dependence to the model that captures the essence of the observed Cl loss well. Values of the calculated fractional yield for the two different models are shown in Figure 14b. The calculation with $k^{ClOO+NO} = 3 \times 10^{-11}$ lowers the yield by $\sim 15\%$ at $T = 215$ K and $\sim 10\%$ at $T = 220$ K, with respect to the model using $k^{ClOO+NO} = 0$.

In summary, there is strong evidence from the flight data that the conversion of ClO to Cl requires the addition of an added loss process due to the presence of ClOO that lowers the calculated yield. Typical values of the yield for ClO measurements range from 0.65 to 0.75. Values of the yield used for the $ClOOC$ and $ClONO_2$ are not affected by the inclusion of the ClOO mechanism, since the temperature in this region of the duct is much greater and ClOO thermal dissociation (6) dominates. The importance of this newly understood systematic error is magnified in the SOLVE chlorine dimer analysis since the analysis goes as the square of the ClO concentration.

In a parallel effort we have begun work to measure the value of $k^{ClOO+NO}$ in the laboratory. The experimental strategy for validating the importance of the ClOO mechanism

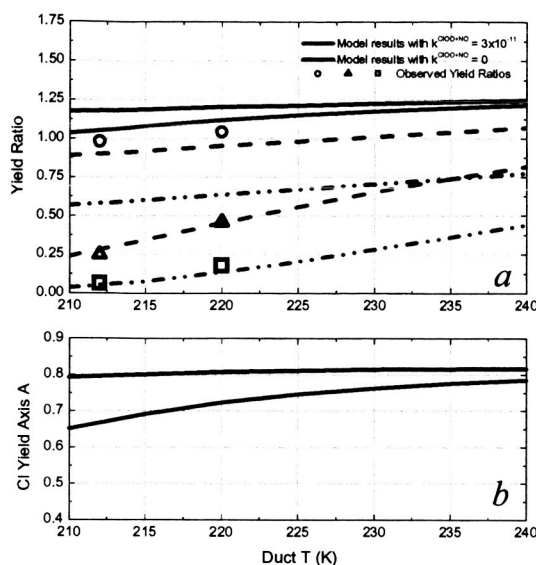


Figure 14: (a) The observed (symbols) and modeled (lines) yield ratios (see text for details) versus Duct T (K) for data from the 0305 flight. Observations are for data at $T = 212$ K (~ 42000 s UT) and $T = 220$ K (~ 52000 s UT). Symbols represent the ratio of observed Cl signals for the following NO flow rates (sccm): 0.18/0.60 (circle), 0.18/3.9 (triangle), and 0.18/7.9 (square). Three sets of lines for two different model runs are shown for $k^{ClOO+NO} = 3 \times 10^{-11} \text{ cm}^3 \text{ molec}^{-1} \text{ s}^{-1}$ (red) and $k^{ClOO+NO} = 0$ (blue). (b) The model calculated Cl yields at Axis A versus T . The effect on yield for the two different models is illustrated.

involves analyzing chlorine atom loss in a kinetic flow system in the presence of NO and N₂ versus the Cl loss in the presence of NO, N₂, and O₂. When O₂ is included as a fraction of the third body concentration, reactions (5, 6, and 7) become important. From the equilibrium constant for ClOO formation, it is known that only a small percentage of Cl will be lost to ClOO (3% at 65 torr and 220 K), so any large differences between the Cl atom loss observed in NO and N₂ versus NO, N₂, and O₂ must be due to the ClOO + NO reaction (7).

The results of the laboratory kinetics study show a clear and dramatic difference between the rate of Cl atom loss due to NO in the presence of nitrogen versus that in the presence of nitrogen and oxygen. This is depicted in Figure 15, where the ratio of the observed rate constants in N₂ + O₂ and N₂ alone are plotted as a function of flow temperature for 10%, 20%, and 30% O₂. The observed Cl atom loss is significantly greater the more O₂ is present and the colder the flow temperature is maintained. At ~ 215 K in the presence of 30% O₂, the observed rate constant is ~3.5 times greater than that in a pure nitrogen carrier gas. The ClOO + NO mechanism is the only known explanation for these large Cl losses observed in the presence of oxygen. This result, along with evidence from the flight data analysis (Figure 14), serve to verify that the ClOO mechanism is an important source of Cl loss in the flight instrument. Pending further laboratory kinetic studies in which ClOO can be measured directly, $3 \times 10^{-11} \text{ cm}^3 \text{ molec}^{-1} \text{ s}^{-1}$ is the current best value for the rate constant of (7) at typical flight temperatures.

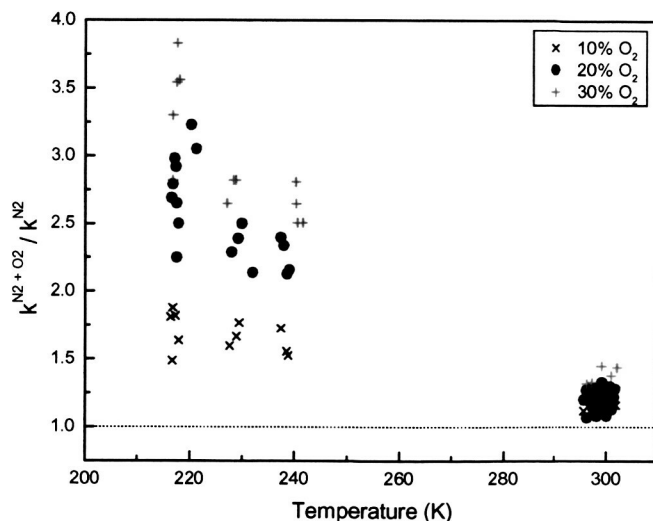


Figure 15: Ratio of observed rate constants for chlorine atom loss due to NO in the presence of nitrogen and oxygen and in the presence of nitrogen only. Data are shown at various temperatures and fractions of O₂ (10%, 20%, and 30%). The dotted line at 1.0 represents no difference in the Cl loss when O₂ is present.

9. Analysis of NO₂ exchange and the evolution of ClO/ClONO₂/NO₂ during SOLVE

Extensive *in situ* observations of NO_x [NO + NO₂], ClO_x [ClO + ClOOCl], ClONO₂, O₃, temperature and pressure in the polar vortex during the SAGE III Ozone Loss and Validation Experiment (SOLVE) were used to study NO/NO₂ exchange and ClO/ClONO₂/NO₂ exchange over a large range of ClO mixing ratios (75–1400 pptv). The observed large range of mixing ratios of ClO, ClONO₂, NO₂, and NO over a three-month period together with the reanalysis of NO₂ mixing ratios following post-flight calibration allowed the quantitative study of the above systems.

To achieve the sensitivity required for observation of the extremely low (< 5pptv) NO₂ mixing ratios in the polar vortex during SOLVE, Avalanche Photodiode Detectors (APDs) were introduced as replacement of the Photomultiplier Tubes used during POLARIS. The APDs

required a detailed characterization of the nonlinear response curve. The LIF sensitivity as a function of pressure and temperature was then measured relative to the N₂ Raman signal, which reflects the counting efficiency of the detection axis, and allows the calibration to be tied directly to the N₂ Raman signal measured during SOLVE. During the course of the calibration possible spectral interferences from other species such as H₂O, CO₂ and O₃ were investigated. It was determined that introduction of O₃ can result in the production of NO₂, probably via reaction with N-containing species on exposed metal surfaces. This may explain the observation of a consistent 14–15 pptv offset of the measured NO₂ mixing ratio during SOLVE, which we have subtracted in our analysis.

A detailed knowledge and understanding of the NO/NO₂ ratio is important in the quantitative analysis of O₃ production and destruction mechanisms. Data from SOLVE allows the first analysis of this ratio under low-NO_x, high-ClO conditions. The measured NO₂ (and HNO₃) in the polar vortex demonstrated severe denitrification and NO₂ mixing ratios below the detection limit (5 pptv in 10 sec.) were encountered. The NO/NO₂ ratio was analyzed using a photochemical steady-state model for NO₂ using JPL-00 recommended reaction rates:

$$^{ss}\text{NO}_2 = \frac{(k_{\text{NO}+\text{ClO}} [\text{ClO}] + k_{\text{NO}+\text{O}_3} [\text{O}_3]) [\text{NO}]}{J_{\text{NO}_2}} \quad (1)$$

A comparison of ^{ss}NO₂ with measured NO₂ for the flight of March 11, 2000 is shown in Figure 16a.

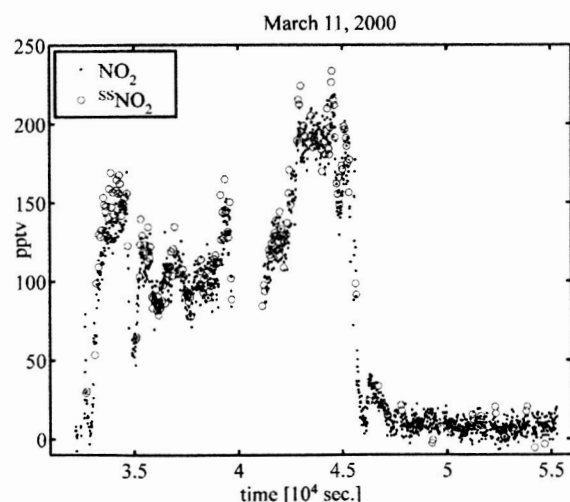


Figure 16a

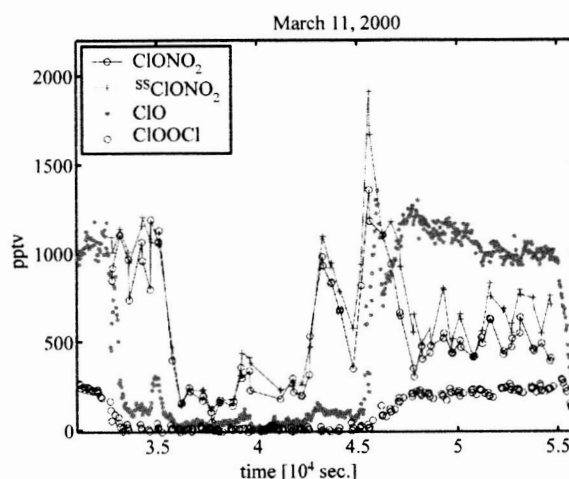


Figure 16b

Figure 16: A comparison of ^{ss}NO₂ calculated with a photochemical steady-state model and observed NO₂ is shown on the left hand side for March 11, 2000. The ^{ss}NO₂ data within the vortex corresponds to 60 s averages. The right hand side shows a comparison of ^{ss}ClONO₂ calculated with a photochemical steady-state model and observed ClONO₂. Also shown is the wide range of ClO and ClOOCl mixing ratios.

The contribution of the ClO + NO reaction to the total NO₂ production increases dramatically from its extra-vortex value of ca. 20% to over 95% within the vortex. Calculated and observed NO₂ agree well up to ~ 90% NO₂ production from ClO (rest from O₃ + NO reaction). Above this the NO₂ and NO measurement errors are large and the NO/NO₂ ratio also is very sensitive to the subtracted offset.

The NO₂ measurements allow comparison of ^{ss}ClONO₂ calculated from a photochemical steady-state expression using JPL-00 recommended reaction rates with measured ClONO₂:

$$^{ss}\text{ClONO}_2 = \frac{(J_{\text{ClONO}_2} + J_{\text{Cl+NO}_3})[\text{ClONO}_2]}{k_{\text{NO}_2+\text{ClO}}[\text{ClO}][\text{NO}_2]} \quad (2)$$

A comparison of $^{ss}\text{ClONO}_2$ with measured ClONO_2 for the flight of March 11, 2000 is shown in Figure 16b. Calculated and observed ClONO_2 agree well (13%) up to a mixing ratio of ~ 1150 ppt ClO . The good agreement indicates that errors in observed ClONO_2 are not large enough to address discrepancies in the chlorine budget during SOLVE.

10. Chlorine-catalyzed polar ozone loss

Rapid catalytic destruction of ozone took place during the second ER-2 deployment of the SOLVE (SAGE III Ozone Loss and Validation Experiment) mission. Losses exceeding 60% were observed in the lower stratosphere of the Arctic vortex (Newman *et al.*, 2002). Data from the 0311 flight further make the case linking stratospheric chlorine to ozone destruction, as shown in Figure 17. ClO and O_3 are plotted as a function of latitude, where the lower latitudes sampled by the ER-2 were in extravortex air, and the higher latitudes were in intravortex air. Upon entering the vortex, the ClO concentration rises sharply, the O_3 concentration falls, and there is a clear anti-correlation in their abundances.

11. Costa Rica progress report

The CWVCS (Clouds and Water Vapor in the Climate System) aircraft mission out of Costa Rica in the summer of 2001 brought a suite of instruments to the tropical tropopause region, with the goal of obtaining detailed, fine-scale *in situ* observations of dessication occurring as air ascends into the stratosphere. Because stratospheric water content closely parallels the average value set by tropical cold point temperatures, it is tempting to view the dessication of that air as a relatively straightforward process. The actual mechanisms driving condensation and evaporation in the upper troposphere, however, can be locally very complex. During CWVCS, NASA's WB-57 high-altitude research aircraft flew a total of seven flights carrying a payload including instruments measuring water vapor, total water (vapor and particles), ozone, temperature, and pressure as well as a high-resolution radiometer. Aircraft flights intercepted a range of conditions from clear air to thin cirrus to tropical deep convective systems. Observations during CWVCS did in fact show that local tropopause temperature can at times exert only a weak influence on near-tropopause water content. In the summertime eastern tropical Pacific, near-tropopause water vapor responded to a variety of controls, none of which were local time-averaged tropopause temperature.

During many flights, observations implied that near-tropopause desiccation could well be temperature-controlled, but not in a simple way. Desiccation is apparently spatially quite heterogeneous, and local water vapor mixing ratios are often controlled by minimum temperatures encountered elsewhere. Many CWVCS flights showed a severely undersaturated upper troposphere, implying that water content is set by conditions elsewhere in the tropics.

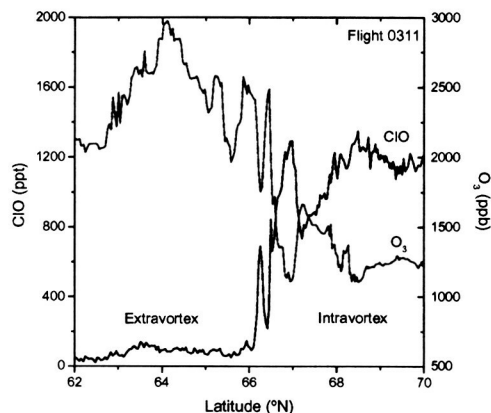


Figure 17: Observed mixing ratios of ClO and O_3 as a function of latitude for the SOLVE flight of 0311. The vortex edge is located $\sim 66^\circ \text{N}$. The ClO mixing ratio is much higher and O_3 is much lower in intratropics air. There is a striking anti-correlation in the abundances of ClO and O_3 in the vortex edge and intratropics regions.

Desiccation may also be time-variable. CWVCS flights showed variation of local tropopause temperatures by as much as eight degrees over the course of a three-week mission, with local desiccation occurring only during episodic cooling of the tropopause. And even when local condensation occurs, water vapor content may not be a simple function of temperature. Flights through near-tropopause cirrus clouds inevitably recorded humidities above saturation, with water vapor mixing ratios extending from near saturation to the limit for homogeneous nucleation. And finally, CWVCS flights showed many instances when tropopause temperature was simply unimportant for stratospheric water content. In the stratosphere proper, the WB-57 made multiple passes through residues of overshooting convective events that pass the tropopause and deposit excess water in the stratosphere, presumably in the form of evaporating ice.

Fine-scale observations such as those obtained during CWVCS imply that many factors are important in determining the ultimate water vapor concentration of stratospheric air. Stratospheric water content is influenced by regional temperature differences, by episodic temperature fluctuations, by microphysics within near-tropopause cirrus, and by the properties of cumulus anvils. Each of these processes can introduce deviations in water content of a factor of two or more. Given the observed variability of these small-scale processes it is remarkable stratospheric water vapor mixing ratios follow as simple a relationship to mean tropical tropopause temperatures as they do. Understanding how the varied processes at work in the uppermost troposphere nevertheless combine to produce a relatively stable and predictable stratospheric water content is a major research priority.

Background

The CWVCS flights were made at a time and place where the tropical tropopause is relatively warm but deep convection is frequency and vigorous. The summertime tropopause over Central America is one of the warmest parts of the tropical tropopause, with average cold-point saturation mixing ratios of 11 ppm, considerably higher than the mean summertime stratospheric water content. The area is, however, located at the peak of inter-tropical convergence zone activity at that time, and cumulus towers regularly reach up to the tropopause and beyond. During CWVCS flight planning, it was expected that detrainment from cumulus towers would provide a substantial amount of near-tropopause cirrus. The flights therefore provided an opportunity for observing many different processes affecting the near-tropopause water vapor content.

The WB-57 aircraft made a total of fifty tropical tropopause crossings during the seven CWVCS flights between August 4 and 18, 2001, returning data on tropopause structure, water vapor, and total water (vapor + condensate). Cirrus ice content was determined by the difference of the vapor and total water measurements. The data returned show remarkable variability in near-tropopause water vapor. Water vapor at the cold-point tropopause differed by a factor of three from crossing to crossing, with much of the variation only weakly correlated with tropopause temperature. (Relative humidities at the cold point themselves ranged from 40% to 160%). Some of the variation in water vapor was related to a distinct cooling of the tropical tropopause that occurred midway through the CWVCS mission; because of this we discuss data from the first and second phases of the mission separately. In general, the CWVCS data provide a rich set of examples of different processes that affect near-tropopause water content. The various processes we infer from this data are discussed in detail in the sections that follow.

Spatial heterogeneity of dessication

During the first phase of CWVCS, tropopause temperatures were typically too warm to dehydrate air to observed stratospheric values. Most aircraft flights in this phase observed a

substantially undersaturated upper troposphere, with water vapor content apparently set by conditions not seen over Costa Rica. Tropopause crossings during the early part of CWVCS often revealed a deep dry layer of air with near-stratospheric water vapor content (7 ppm) extending several km into the near-tropopause region, as deep as the 360 K potential temperature surface. Figure 18 shows a typical profile of this type. The mean water vapor content of the lower stratosphere (385–400 K θ) measured during CWVCS is 6.7 ppm, a typical summertime value. The tropopause itself was often difficult to define in this period, with the temperature profile nearly isothermal over several km, though laced with multiple small temperature inversions and local cold points. The near-tropopause region in these profiles resembles a classic transition region, with both ozone and potential temperature gradually increasing to stratospheric values; the standard WMO tropopause definition is not a particularly useful concept here. Figure 19 shows data from about two-thirds of the profiles in the first CWVCS phase, those obtained well away from local convective systems; the data span three separate WB-57 flights. The figure shows temperature, water vapor, and relative humidity at the location of minimum saturation mixing ratio, i.e., the locations of maximum dessication potential. All show remarkably consistent near-tropopause water content of about 7 ppm. It is clear that local conditions are not capable of drying air to that extent.

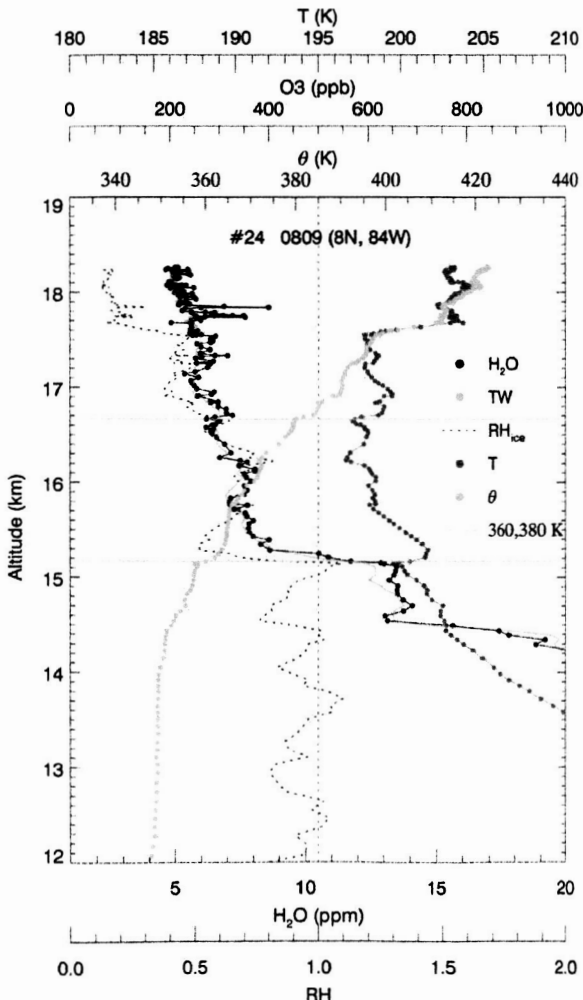


Figure 18: A typical profile from the first half of CWVCS, with a deep dry layer of air filling the uppermost troposphere. The horizontal blue lines represent the 360 and 380 K potential temperature surfaces, marking the approximate boundaries of the tropopause transition layer (TTL). The temperature profile (in orange) is nearly isothermal through this layer, albeit with much small-scale structure. On this ascent the aircraft rose through heavy cloud into light haze, and the troposphere remains saturated up to the base of the TTL (the blue dotted line sits at $S = 1$), though there is no detectable cirrus present. (Total water, in green, is indistinguishable from water vapor, in black). Note the abrupt distinction between this saturated region and the undersaturated TTL above.

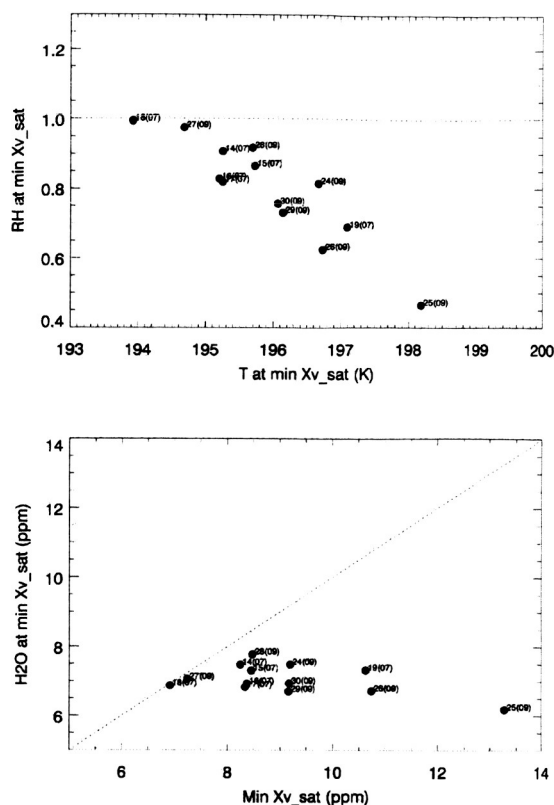


Figure 19: Relative humidity and water vapor content at the tropopause for those profiles in the first phase of CWVCS that show a deep dry near-tropopause layer (approximately 2/3 of the total profiles). For this purpose the tropopause is defined not as the cold point but as the location where saturation mixing ratio is minimum, i.e. the location of maximum potential dehydration. The number beside each data points is the index of the tropopause crossing (sequentially out of 50 during CWVCS); the number in parentheses is the day in August 2001 that crossing occurred. Tropopause water vapor mixing ratios were consistently near 7 ppm for this set of tropopause crossings, regardless of the local tropopause temperature. Tropopause relative humidity is therefore simply a function of tropopause temperature.

The upper troposphere is not completely immune from local influence during this phase of CWVCS. The remaining third of the tropopause crossings from this phase were made near or directly above local convective activity, and these profiles do show the influence of convection (Figure 20). The eight "convective" profiles in Figure 20 include the last dive and descent into Juan Santamaria Airport, Costa Rica on August 4, when the pilot noted descent through thick cloud; four dives from August 7 made around a small convective system that was generating strong gravity-wave activity in the lower stratosphere, and a descent made on August 9 through the outflow of a convective system. In all these cases, evaporation of detrained ice has presumably raised upper tropospheric water vapor, bringing it up to saturation (or even slightly beyond it). These profiles were made in clear air: to the precision of the total water instrument there is no detectable cirrus. Evaporation of particles is presumably complete by the time the aircraft intersects the air parcels. Where convection does play a role in setting near-tropopause water content, it acts to increase water content, bringing it up to local saturation. There is no evidence that convection produces local cold temperature anomalies that can dessicate air beyond the values implied by the mean tropopause temperature. The cold point temperatures observed in dissipating convective systems are in fact higher than those well away from convection. Convective activity in this region then serves only to bring near-tropopause water content up to local saturation, that is, to moisten it to well above stratospheric values.

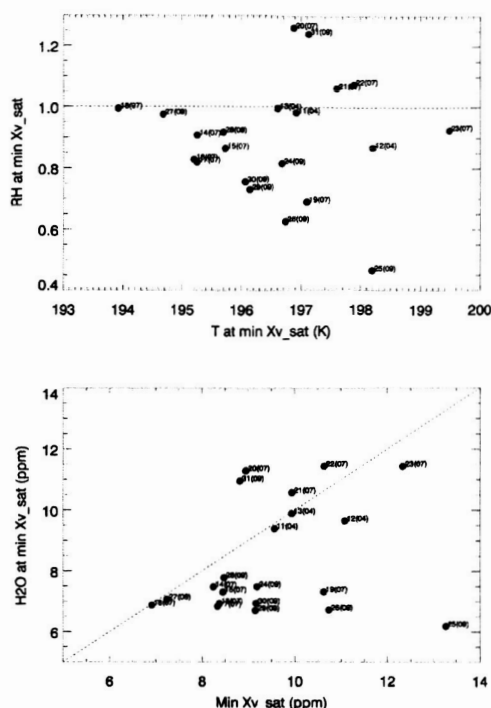


Figure 20: Relative humidity and water vapor content at the tropopause for all profiles measured in the first phase of CWVCS, as in Figure 19. The dry-layer profiles of Figure 19 are shown in black; profiles obtained near convective systems are added in red. Convection acts to bring the undersaturated air up to local saturation or even a bit beyond it.

It should be noted that the proportion of profiles from CWVCS that show convective influence is almost certainly biased high. The WB-57 pilot was actively searching for near-tropopause outflow cirrus and so was seeking out convective systems. Although local deep convection is seen to modify the near-tropopause water vapor content in this part of CWVCS, the influence is relatively small. For the most part, the upper troposphere shows water vapor mixing ratios far below values that can be locally determined. We conclude that the dessication of near-tropopause air to stratospheric values is largely happening elsewhere, and that dry air is then advected horizontally into the warmer Eastern tropical Pacific. The region of drying may be the Western Pacific, since winds in the layer just below the tropopause (360 to 380 K θ) were largely westerly during CWVCS (in contrast to the prevailing easterlies in the stratosphere proper and in the tropopause below). The predominant undersaturation in the uppermost troposphere during the first phase of CWVCS explains why we observed no outflow cirrus there, despite strong local convective activity. When ice particles are detrained into strongly undersaturated air, evaporation is swift and the resulting cirrus lifetime is short. Where local convection occurs in the Eastern tropical Pacific, then, it serves to re-moisten the air. That convection evidently does not provide enough mass flux to overwrite the drier signal stamped on upper tropospheric air by other regions. In this phase of CWVCS, the near-tropopause water vapor in the Eastern tropical Pacific was governed by non-local processes.

Hydration of the stratosphere by deep convection

The same moistening effect of convective detrainment that is observed in the troposphere was also seen in the stratosphere proper. Throughout CWVCS, WB-57 flights intercepted periodic incursions of much wetter air in the stratosphere (9–11 ppm) that we interpret as the evaporated residues of overshooting cumulus turrets. Figure 21 shows a typical such event, observed on August 9, with three individual layers of enhanced water visible between 380 and 390 K θ . Similar stratospheric layers with enhanced water vapor were commonly found just

above the tropopause and, less commonly, as high as 420 K θ . The distribution of altitudes is high for deep convection but not unprecedented.

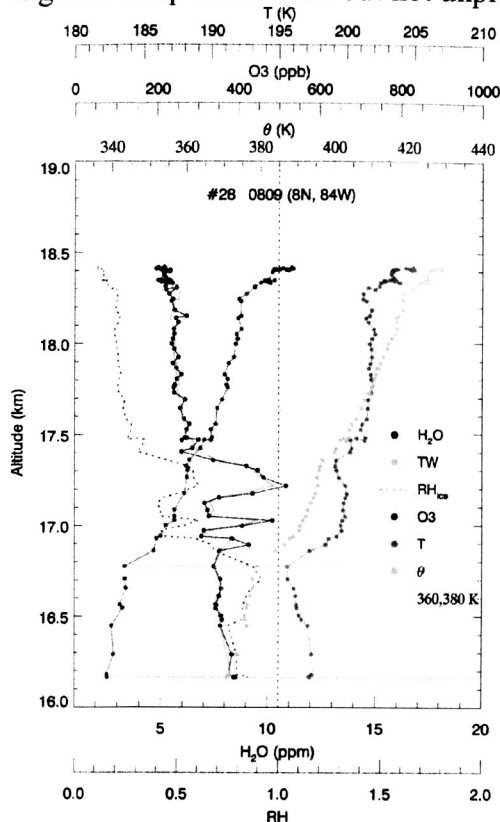


Figure 21: A typical profile obtained during CWVCS showing convectively generated water vapor enhancements in the stratosphere proper. In this dive the aircraft encountered three thin layers of air in which water vapor nearly doubled from 6 to 11 ppm (black, green lines). The enhancements lie well above the 380 K θ surface (shown as a blue horizontal line). In this case the convective anomalies were associated with slightly elevated temperature and ozone (in orange and pink, respectively). However, there is no consistent pattern throughout the campaign, and the reverse can also be true. Relative humidities are necessarily elevated in the wetter layers, but remain well below saturation (blue dotted line).

The sharpness and the altitude distribution of the water vapor enhancements mean that they must be convective in origin. The amount of water observed alone is not incompatible with passage of some air through a warmer, wetter, tropopause. Bringing water content to 11 ppm from the average observed value of 6.7 ppm would require a coldpoint temperature increase of only 2.5 degrees. However, it is not possible that those inhomogeneities would persist undiluted and unmixed for the over two months required to ascend to the maximum altitude of observed stratospheric enhancements. The water vapor anomalies are also spatially very restricted. This is best seen on the flight of August 9, when the WB-57 encountered narrow tongues of enhanced stratospheric water vapor while making a series of three "stack flights". In each of the stacks, the aircraft made repeated level N-S traverses of 150 km over the same ground, covering a range of altitudes from 16 to 18 km (375–433 K θ). The stacks themselves were separated E-W by 100 km. The flight pattern thus allowed determination of both horizontal and vertical structure of the water vapor enhancements. Those tongues were as little as 40 km in horizontal extent (N-S) and 100 m vertically. In the E-W direction, tongues seen on the eastern stack were not observed on the western stack two hundred km away. We believe that this degree of spatial structure cannot be maintained against mixing and stirring during gradual ascent in the stratosphere. The most likely candidate for the origin of these tongues is a strong convective system that had developed a few hundred kilometers east of the flight track on the previous day. Prevailing easterly winds would have carried that air into the flight path overnight.

There has been much debate in the last several years about the effect of tropical deep convection on the stratosphere proper—whether it acts to hydrate or dehydrate the stratosphere—and arguments have been made in both directions. The CWVCS data imply that, at least in the

Eastern Pacific, convection acts only to moisten the stratosphere. We saw no instances of negative anomalies in water vapor in the stratosphere proper, i.e., no incursions of air that was drier than average. The sole convective anomalies observed were wet ones. During the first phase of CWVCS, outflow from convective systems both in the troposphere and the stratosphere would be made into strongly undersaturated air. The CWVCS data suggest that the outcome was, not surprisingly, rapid evaporation of particles and addition of moisture to the air.

Convection that deposits evaporating ice directly into the overworld stratosphere represents a conduit for water to reach the stratosphere without being limited by tropopause temperatures. "Unchecked" processes such as this, if significant to the stratospheric water vapor budget, could potentially allow large changes in stratospheric water content under future climate regimes. The CWVCS data suggest that such channels do play some role in setting the final stratospheric water content, though it is not yet clear how important that role is for the overall mass budget of water vapor reaching the stratosphere. Determining that importance is thus a priority for future research.

Time-variability of cold-point temperatures

During the second half of the CWVCS mission, the tropical tropopause underwent a significant change on a global scale that produced local effects on upper tropospheric water vapor. Beginning in mid-August 2001, intense convection in the Western tropical Pacific pumped heat into the atmosphere and effectively raised the tropopause altitude throughout the tropics; cold-point tropopause temperatures correspondingly dropped by several degrees. This phase of a higher and colder tropopause endured for approximately two weeks, and CWVCS fortuitously caught the beginning of it on the last two flights of the campaign. The difference in atmospheric structure during this time goes well beyond normal day-to-day variability. The change is readily apparent in the atmospheric structure recorded by the WB-57 instruments (Figure 22). Although the cold-point tropopause did not change in potential temperature, the potential temperature surfaces are effectively elevated, producing tropopause temperatures on average five degrees colder.

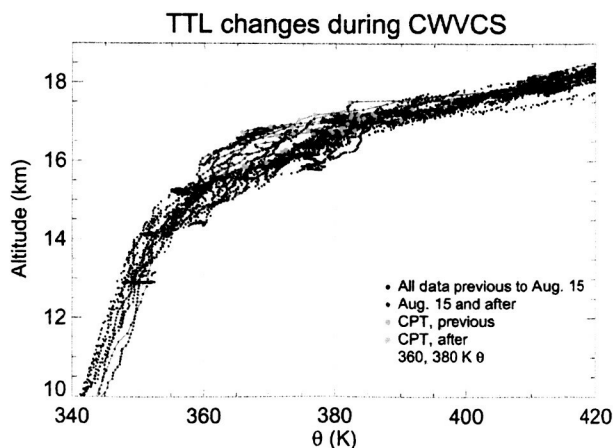


Figure 22: Atmospheric structure during CWVCS. The second half of CWVCS saw a warming of the free troposphere and lifting of the isentropes, with a consequent lifting and cooling of the tropopause. The black points in this profile represent the atmospheric structure seen in the first phase of the mission, with the green dots the cold-point tropopause observed on each tropopause crossing. The red lines represent the second phase of the mission, with the local tropopause given by blue dots. Note that the mean tropopause potential temperature does not change in the second half of CWVCS, but the lifted isentropes produce colder temperatures and thus lower saturation mixing ratios and increased potential for dessication. Reanalysis data show similar structural changes throughout the tropics at this time.

The combination of a tropopause both higher and colder necessarily means that it must be sharper. During the second phase of CWVCS, the near-isothermal upper tropopause temperature profiles of the first half of CWVCS were replaced by much sharper transitions. Figure 23 shows the most extreme of these profiles, with an abrupt temperature leap of 8° between the upper troposphere and lower stratosphere. This profile contains considerably drier air than had ever been observed in the first half of the mission, and shows evidence of local removal of water from near-tropopause air. The aircraft crossed two thin layers of cirrus immediately below the

tropopause, obvious in this figure as the places where total water (in green) diverges from water vapor (in black). The peaks of total water concentration are shifted slightly downward from the corresponding water vapor minima, suggesting sedimentation of ice crystals. The apparent descent of particles leaves residual air whose total water content is diminished. At the top of the highest cirrus layer, air has been dehydrated irreversibly to nearly 5 ppm.

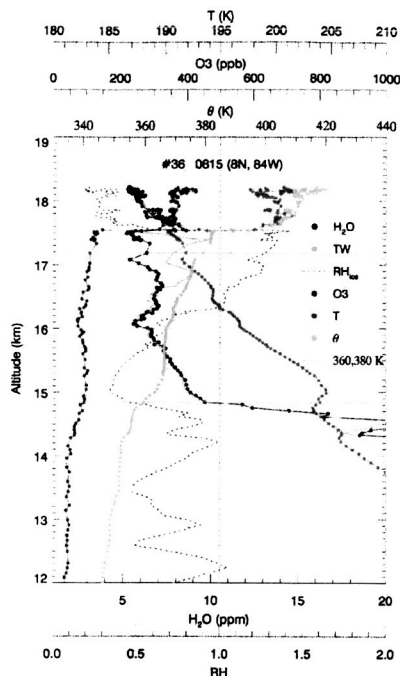


Figure 23: The first ascent of the WB-57 during the second phase of CWVCS, showing a very high, very sharp tropopause. Near-tropopause cirrus is now readily apparent (separation of green total water line from black water vapor), and a layer of supersaturated air extends for a kilometer below the tropopause. The patterns observed during previous CWVCS flights are not completely eradicated, however. There remains, as in Figure 22, a sharp distinction between the bulk of the troposphere and the TTL above it, again with a boundary marked by an abrupt transition to lower water content. In this profile though further irreversible dehydration has occurred, bringing total water content down to 5 ppm in places.

In the first phase of CWVCS, the tropopause was generally warm and undersaturated, with occasional excursions to warm and saturated. In the second phase, the tropopause is cold and hovers slightly above saturation. (The excess over saturation is discussed more fully in the section below). Figure 24 shows the full set of CWVCS tropopause crossings; the difference between the first and second phases is apparent. Note that although relative humidities are high in the second phase, specific humidities are actually lower. During the first phase, the tropopause neared saturation only when local convection acted as a source of water vapor, moistening a previously undersaturated upper troposphere. In the second phase, it is temperature rather than water content that changes, with the temperature reduction bringing the upper tropospheric saturation mixing ratios to below the prevailing water content, so that water is subsequently removed. The tropopause crossings in the second phase of the mission imply a net reduction of moisture rather than a net addition.

The frequency of cirrus detection differs strongly between the first and second phases of CWVCS. While the WB-57 observed only clear air during tropopause crossings in the first phase of CWVCS, from takeoff on August 15 until departure from Costa Rica the plane never again made a tropopause crossing without detecting cirrus. All the observed cirrus was clearly convective outflow rather than *in situ* condensation, because its total water content is well above the previously seen background water level. There is no evidence for any change in convective frequency during these later flights. The occurrence of convection in satellite images, or of convective residues observed by the WB-57 in the stratosphere, remains similar. What changed was instead the background into which convective detrainment occurred. Because

tropopause cooling had brought the background air into supersaturation, the evaporation of outflow cirrus was inhibited and cirrus lifetime extended, allowing the aircraft to sample it.

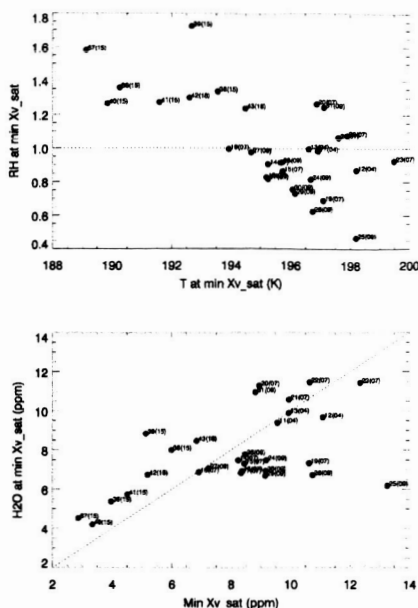


Figure 24: Relative humidity and water vapor at the tropopause during all of CWVCS. Tropopause crossings from the first half the mission are shown in black, and from the second half in red. The cooling of the tropopause during the second phase is apparent. This cooling means that minimum saturation mixing ratios now drop below the characteristic 7 ppm water content of the uppermost troposphere in the first phase. There is little possibility of undersaturation now, and in fact observations at the new, colder tropopause all reveal water vapor near or above saturation. Local convection can therefore have little further impact on the water content of the uppermost troposphere.

The data obtained during the second phase of CWVCS suggest that even in a warm-tropopause region, some local removal of water can occur during episodic cooling events. Again, it is as yet unclear how this contributes to the mass balance of water vapor entering the stratosphere. NCEP reanalysis data suggest that coolings of the type seen during CWVCS are low-frequency events, occurring once or twice in a summer. But the observations serve as an example demonstrating that the dessication of near-tropopause air can vary temporally as well as spatially. The cold-traps that remove water vapor from near-tropopause air are not necessarily fixed.

Supersaturation in the presence of cirrus particles: inefficient dehydration

The cirrus observations obtained during the second phase of CWVCS suggest that even when local dehydration in cirrus does occur, it may not be as efficient as would be predicted by simple condensation models. The idea of cold-trapping of air entering the tropopause depends on the assumption that the Clausius-Clapeyron equation holds, and that "saturation" is a limit to the amount of water vapor that air will hold. Although clear air can maintain some degree of supersaturation, microphysical models generally predict that once droplets or particles first nucleate, the water vapor content of the surrounding air is driven quickly down to saturation. During CWVCS, however, supersaturations greater than 1 were routinely observed in thin cirrus near the tropopause. While clouds observed at lower altitudes (below 16 km) invariably held water vapor at saturation, average cirrus supersaturation level was about 1.3. Figure 25 shows the distribution of relative humidities observed in clear air and in cirrus during CWVCS.

The observations of cirrus supersaturation during CWVCS are well-supported, and we are confident in ruling out instrumental effects. Calibration of the instrument is not a factor, since saturation is consistently observed in thicker clouds below. For the same reason, contamination of the data by evaporating cloud ice cannot explain the data; contamination should be a larger problem in thicker clouds. Observations during the CRYSTAL-FACE campaign in 2002 also provided confirmation that the contamination effect was restricted to a few percent at most. The temperature measurement on the WB-57 has been cross-calibrated against the MMS system that

flies on both the ER-2 and WB-57, and the two measurements agree to better than a half degree. These issues are discussed in more detail in Smith *et al.* (2005).

If instrumental error is ruled out, the explaining the CWVCS observations requires a physical mechanism that slows the condensation of water molecules onto cirrus particles so that high supersaturations can persist and be observed. Understanding of cirrus microphysics during CWVCS is limited by the lack of particle size distribution measurements on the CWVCS payload, but some plausible microphysical scenarios can be developed using our measurement of total ice water content and estimates of particle size distributions. Preliminary model results suggest that if near-tropopause cirrus consists of anvil outflow cirrus, as it seems to, with particle sizes in the 1 to a few micron range, and that outflow is seeded into previously supersaturated air, supersaturations can persist for as much as an hour (Thomas Peter and Stephen Fueglistaler, personal communication). Many WB-57 cirrus observations, including those with the highest levels of supersaturation, are considerably younger than that. The highest supersaturations were observed when the pilot flew directly through blowoff from a just-risen near-tropopause anvil cloud. The age of the cirrus shown in Figure 23 cannot be readily determined, but a timescale of an hour is not unreasonable. Though more modeling is clearly necessary, the observations obtained during CWVCS are physically plausible.

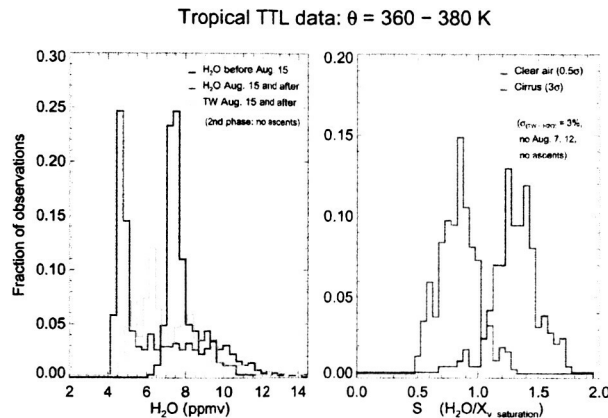


Figure 25: Histograms of relative humidities and water vapor content of air in the TTL (defined as the region bounded by the 360 and 380 K θ surfaces). The left panel shows changes in the distribution of water vapor in the TTL from the first phase of CWVCS (black) to the second (blue). The mode of 7 ppm water vapor is shifted down to 5 ppm. It is true that many of the second phase observations were made in the presence of cirrus particles, which could later re-evaporate and partially restore water to its previous value. To demonstrate that much of the dehydration is in fact irreversible, total water in the second phase of CWVCS is plotted in light blue. Even with cirrus particles taken into account, air in the second half of the mission is drier. The data plotted here include all TTL data points excluding only ascents out of Juan Santamaria airport, where contamination of the inlet produced temporary offsets in measured total water. The right panel shows relative humidities observed in clear air and in cirrus. Cirrus points are derived only from the second phase of CWVCS; clear air points may derive from either phase. To accurately differentiate clear from cloud air and prevent instrumental errors from affecting the interpretation of physical phenomena, the data here are binned conservatively and not all data is used. In general total water and water vapor measurements agree to within a standard deviation of 3%. In this figure "clear air" points are taken as those data where water vapor and total water measurements agree to better than $\frac{1}{2} \sigma$. "Cirrus" observations are those data where the water vapor and total water measurements disagree by more than 3σ . With this definition, no significant clear air supersaturation is observed. Air containing cirrus particles, on the other hand, is almost universally supersaturated. The cutoff for maximum supersaturation is, to within instrumental accuracy, approximately that required for homogeneous nucleation of ice particles.

The possibility of substantial supersaturation in near-tropopause cirrus has important implications for stratospheric water vapor. The control of stratospheric water by cold-trapping at the tropical tropopause is considerably less straightforward if water content at a given

temperature may vary by a factor of 160%. Stratospheric water content would then become a strong function of the microphysics of near-tropopause cirrus. The CWVCS observations again point out an area where further studies are critically necessary. It is possible, for example, that the conditions seen over Costa Rica are anomalous. No flight during CWVCS encountered true *in situ*-formed cirrus, for example, whose particle size distribution should be very different, but *in situ* cirrus formation is assumed to be the dominant removal mechanism for upper tropospheric water passing through the Western Pacific cold pool. Water vapor mixing ratios may be limited to saturation in the regions where the bulk of cold-trapping occurs. On the other hand, if high supersaturation were observed in the Western Pacific cold pool, then detailed understanding of cirrus properties and evolution would clearly be necessary to fully understand stratospheric water vapor.

Conclusions

The CWVCS campaign provided a rich dataset of examples of processes that affect water vapor in the near-tropopause region. Specifically, CWVCS observations showed evidence of multiple mechanisms that can weaken the correlation between tropopause temperature and the water vapor mixing ratio of air entering the stratosphere. Non-local desiccation, delivery of water directly to the stratosphere by overshooting cumulus towers, episodic fluctuations in tropopause temperature, and persistent supersaturation in cirrus all complicate the simple picture of cold-trapping at the tropopause as the control of stratospheric water vapor. Each of these provides an additional factor that must be taken into account when predicting the results of any future climate shifts on the stratosphere, and each can make stratospheric water more susceptible to sudden change. Future aircraft campaigns should allow us to begin making quantitative estimation of the importance of each mechanism and of the ultimate robustness of stratospheric water vapor content.

12. Observations of supersaturation in the presence of cirrus in the subtropical upper troposphere: Results from CRYSTAL-FACE

We present *in situ* observations of water vapor and relative humidity with respect to ice, RH_{ice} , in the subtropical upper troposphere obtained aboard the WB-57 aircraft on flights out of Key West, Florida during the CRYSTAL-FACE mission in July 2002. The Harvard water instrument uses the established Lyman- α photo-fragment fluorescence detection technique to make accurate and precise measurements of water vapor in the vicinity of the tropopause. We frequently observe ice-supersaturation both in clear air and in the presence of cirrus. Our clear air observations, plotted in Figure 26a, show that the summertime upper troposphere over south Florida is supersaturated 20% of the time. The in-cloud data are normally distributed with a mean supersaturation of 110%, and over 70% of the in-cloud observations have relative humidities greater than 100%, cf., Figure 26b. Several factors from the direct effects of local convection, to mesoscale meteorological processes and variability in aerosol chemical composition will influence both relative humidity distributions and the degree of supersaturation required for ice nucleation. Flight-to-flight variability in the distribution provides a means of investigating the role of each of these factors. These data present a substantial contribution to *in situ* observations of clear air and in-cloud relative humidity.

The clear air distribution of RH_{ice} decreases exponentially above the equilibrium value of 100%, and there are no instances of supersaturation in clear air above 165%. In contrast, the in-cloud data exhibit a symmetrical distribution centered about a relative humidity of 110%, with values as high as 180% supersaturation. The clear air data are consistent with a maximum ice nucleation threshold of $\sim 160\%$, the level required for homogeneous nucleation of sulfuric acid aerosol. The peak relative humidity in clear air should not exceed this value, and in fact the

distribution of supersaturation above 100% may be used to infer the dominant nucleation mode. Initial results, using the Harvard water vapor data, suggest that heterogeneous nucleation occurs, and may be the dominant mode for initiating cloud formation, however the enduring high supersaturations evident in the in-cloud data suggest that homogeneous nucleation is critical for cloud growth and persistence.

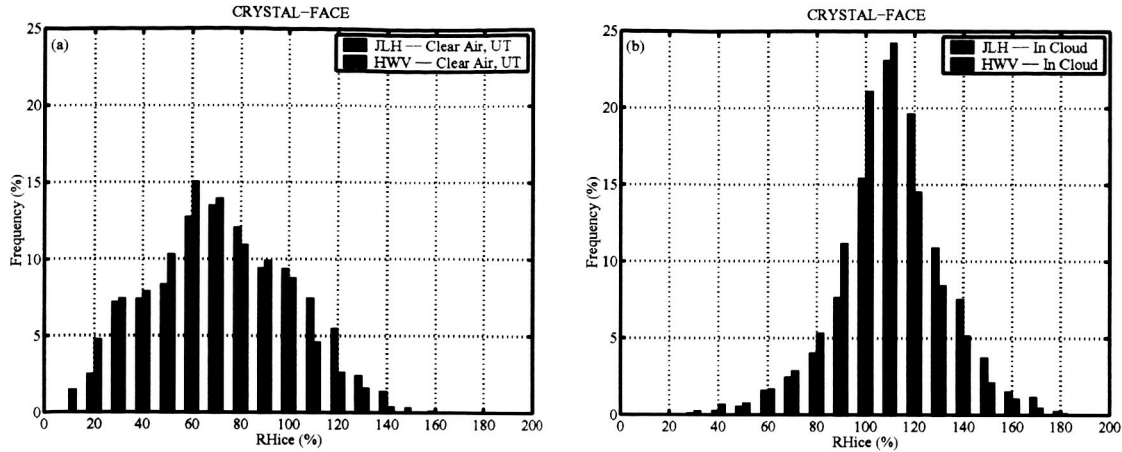


Figure 26: Relative humidity distributions, in clear air (a) and in cloud (b), for the summertime subtropical upper troposphere. In this analysis, clear air is defined as having fewer than 0.01 cm^{-3} $10 \mu\text{m}$ particles, and the upper troposphere (UT) is the region bounded by the 335 and 375 potential temperature surfaces. We have plotted data from both Harvard water vapor (HWV) and the JPL laser hygrometer (JLH) for comparison. The combination of MMS temperatures and Harvard water generally yields the lowest values for RH_{ice} . The combined uncertainty is $\sim \pm 10\%$, where a 0.2 K uncertainty in measured temperature yields a $\sim 5\%$ uncertainty in SMR_{ice} , and the accuracy of Harvard water is $\pm 5\%$.

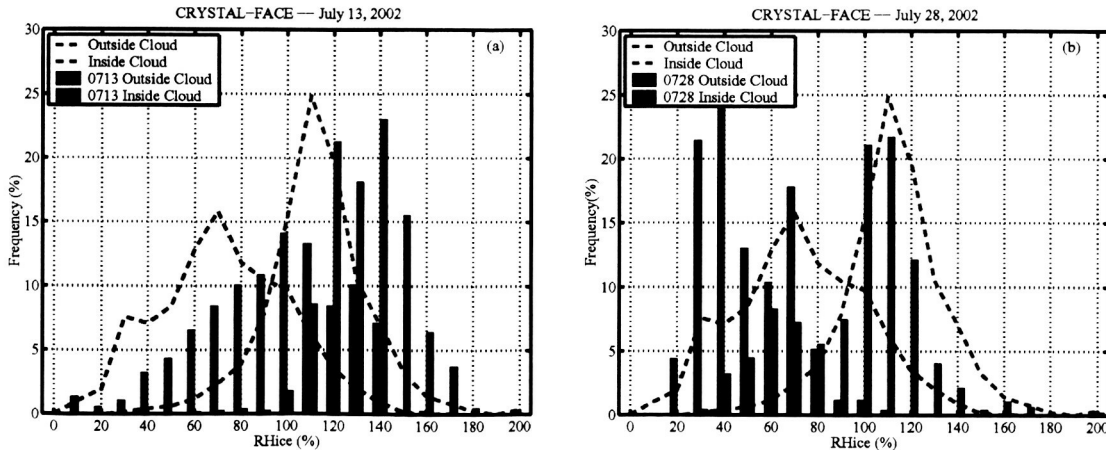


Figure 27: Clear air and in-cloud relative humidity distributions for the flights of July 13, 2002 (a) and July 28, 2002 (b). The clear air and in-cloud distributions for the mission as a whole are plotted for comparison, dashed lines. Both flights show a clear departure from the mission means, to higher and lower relative humidities respectively.

The clear air and in-cloud relative humidity distributions for individual flights over southern Florida are, as a rule, indistinguishable from those representing the mission as a whole. However, the flights of July 13 and July 28 are exceptional. On the flight of July 13, both the clear air and in-cloud relative humidity distributions show a higher frequency of supersaturated air. The clear air data show a notably higher frequency of supersaturation, though the sharp decline at $\text{RH}_{ice} \approx 150\%$ is consistent with the onset of ice nucleation. The in-cloud data from this flight retain a symmetric distribution, though the center is shifted $\sim +20\%$. The opposite is

true for the flight of July 28, where none of the clear air relative humidity values are greater than 120%, and the in-cloud data exhibit a bimodal distribution with a significant fraction of cloud particles present in air that is undersaturated. Through a detailed analysis of the factors controlling the relative humidity distributions on these days in particular, we hope to gain insight into the factors controlling clear air and in-cloud relative humidities more generally.

13. Water vapor and total water instrumentation

We have been flying a photofragment fluorescence hygrometer on the NASA ER-2 aircraft since 1992. The accuracy of that instrument based on pre- and post-mission laboratory calibrations, validated by comparisons with in-flight water vapor measurements by direct absorption, and additionally by intercomparisons with the Jet Propulsion Laboratory near-infrared tunable diode laser hygrometer (May 1998), is $\pm 5\%$, with an offset of at most $\pm 0.1\%$ (Hints *et al.*, 1999). We have recently developed and flown on the NASA WB-57 research aircraft water vapor and total water instruments that use detection axes virtually identical to that used on the ER-2 instrument. The water vapor instrument was integrated to fly in a spearpod with a double-ducted, fast-flow system that allows sampling of the laminar core of the ram-fed ambient air. This ducting differs from that in the ER-2 instrument only with a reduction in duct size from 7.5 to 5 cm rectangular cross section, and with the addition of a U-shaped light trap before the detection axis. The total water instrument, utilizing an identical detection axis, an isokinetic inlet, and heater, is mounted in a pallet in the fuselage of the aircraft. The constraint of isokinetic flow results in mass flow rates at least an order of magnitude slower than that in the water vapor instrument, while the addition of heat results in temperatures at the detection axis being close to 20°C . These two differences are significant when it comes to potential sources of systematic error for the *in situ* measurement of water vapor and accordingly, measurement intercomparison in clear air can be very illuminating and serve as an independent form of validation. We summarize here water vapor instrument calibration issues, validation and calibration issues for the total water instrument, and additionally, laboratory and flight intercomparisons with a JPL diode laser hygrometer that flew on the WB-57 during the CRYSTAL-FACE mission.

Calibration and Operation of the Water Vapor instrument

The water vapor instrument was redesigned for the NASA WB57 research aircraft and flew in the Clouds and Water Vapor in the Climate System (CWVCS) mission in Costa Rica in August 2001 and CRYSTAL-FACE (CF) mission in Florida during July 2002. These last two campaigns focused on the study of cirrus clouds in the upper troposphere and lower stratosphere (UTLS), a new and different environment from previous missions that had a stratospheric focus. Accurate measurements of water vapor and relative humidity in the tropical and subtropical UTLS are crucial in order to improve our understanding of the radiative properties of cirrus clouds, and the processes responsible for their formation and dissipation.

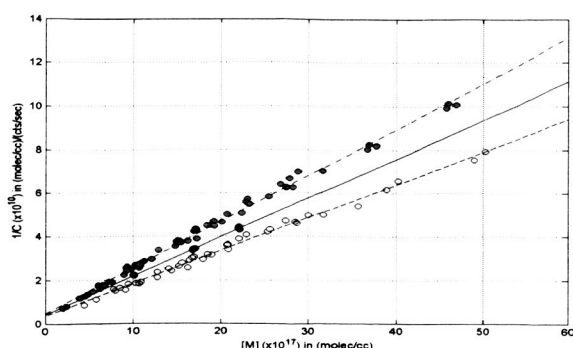


Figure 28: Water vapor calibrations for the CRYSTAL-FACE mission. Plotted is the inverse of the sensitivity of the instrument *versus* ambient density. The cyan points correspond to calibrations performed before CRYSTAL-FACE (March–May 2002). The red points correspond to calibrations performed during CRYSTAL-FACE (July 2002). The yellow points correspond to calibrations performed after CRYSTAL-FACE (August–December 2002). The lines represent the best fit for each set of points (before, during, and after).

During certain flights, we were able to perform calibration checks by comparing water vapor concentrations determined by fluorescence to those measured by absorption. Figure 29 shows one example of this comparison. The result shows agreement between absorption and fluorescence to within 6% when we use the calibration constants obtained during the mission. Thus, performing calibrations in the field proved critical during CRYSTAL-FACE and improved our confidence in our reported water vapor values.

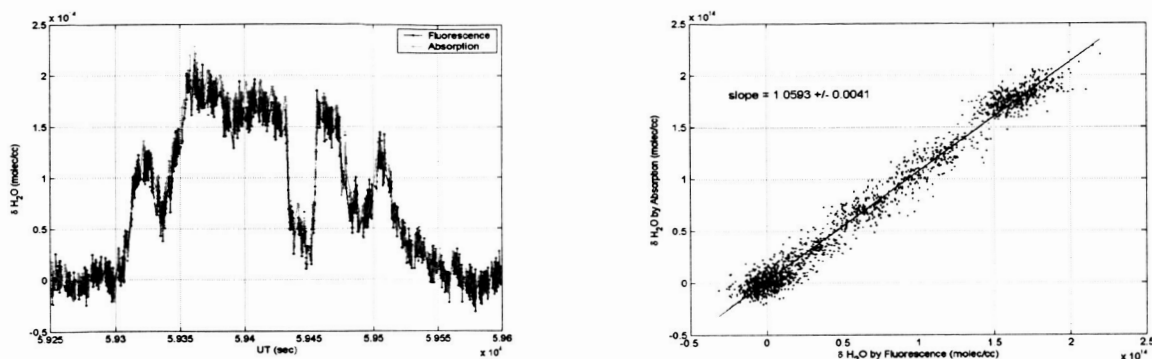


Figure 29: Water vapor concentrations calculated by absorption and by fluorescence on July 27, 2002, during CRYSTAL-FACE.

Accurate quantification of relative humidity is very important for understanding the mechanisms responsible for cloud formation. The issue of potential evaporation of small cloud particles in the duct of the water vapor instrument could have a significant impact on reported relative humidity values. During the Costa Rica mini-mission we frequently observed unusual regions of high supersaturation in clouds (up to 80%) near the tropopause. We explored the possibility of evaporation of ice in the duct by first performing calculations of evaporation times versus residence time of particles in our duct. The results show that the residence time in the instrument is short enough that only particles smaller than $1 \mu\text{m}$ would evaporate. Significant contribution from evaporation in our measurements would require a large number density of these small ice particles, resulting in regions of large optical thickness. These conditions were inconsistent with the observations reported by the pilot. The CF campaign provided the opportunity to further explore the issue of evaporation by comparing our water vapor measurements to those made by JPL's open path laser hygrometer, also aboard the WB-57. Based on this comparison, our instrument shows evaporation of 2–10% of the ice water content. Post-mission analysis shows that this evaporation number is variable and must be determined on a cloud-by-cloud basis. Unfortunately, the JPL instrument did not report data during many transects through thicker cirrus, so comparison opportunities were often limited. Nevertheless, the results from the CF mission allow us to evaluate to what extent, if any, the evaporation of ice particles contributed to the high supersaturation measured in clouds during the Costa Rica mini-mission. For example, when supersaturation levels of 60% were measured in thin cirrus in Costa Rica, the water vapor content was around 5 ppmv, and the ice water content ranged from 3–6 ppmv. In the worst case, if we evaporated 10% of 6 ppmv of ice in a background of 5 ppmv of water vapor, the relative humidity would have been increased by an additional 18% due to the evaporation in the water vapor duct. While this estimate shows the potential impact of evaporation on the measured supersaturation, it does not change the implications of high supersaturation observed in cirrus clouds near the tropopause during the mini-mission to Costa Rica.

Validation of a total water instrument for the NASA WB57 aircraft

The total water instrument combines an isokinetic inlet, a heated duct, and a photofragment fluorescence detection axis to quantitatively measure the total water content of clouds in the upper troposphere and lower stratosphere. When flown with our water vapor instrument, the instrument provides cloud ice water measurements with an accuracy ranging from 5–15%, depending on particle size distributions. The minimum uncertainty is based solely on the uncertainty in the measurement of water vapor in the absence of clouds. The instrument was test-flown during May 2001 in Houston, TX, and then participated in the CWVCS from San Jose, Costa Rica, in August 2001. The instrument also participated in the CRYSTAL-FACE mission in July 2002 flown from Key West, Florida. As with the water vapor instrument, the accuracy that is based on laboratory calibrations taken before, during, and after the mission, can be tested as well by in-flight absorption measurements. Numerous cloud transects during CRYSTAL-FACE provided the opportunity to independently track the sensitivity of the total water detections axis during the mission. We emphasize again that because total water operates at close to room temperature, and under significantly different flow conditions than the water vapor instrument, intercomparison of the two independent measurements of water vapor in clear air provide further validation of the accuracy of the water vapor instrument. It is also necessary to point out that validating the accuracy of the total water measurement in clouds requires it to make accurate water vapor measurements in clear air. The degree to which the instrument exhibits hysteresis directly impacts its accuracy. Limiting this hysteresis requires proper instrument design, with removal of potential sources of water with long time constants, such as real and virtual leaks, and material outgassing. Additionally, the instrument is purged, evacuated, and dried after each flight.

To illustrate instrument capability, we compare and contrast segments of data taken during the flights on August 9 and 15, 2001, in Figures 30 and 31, respectively.

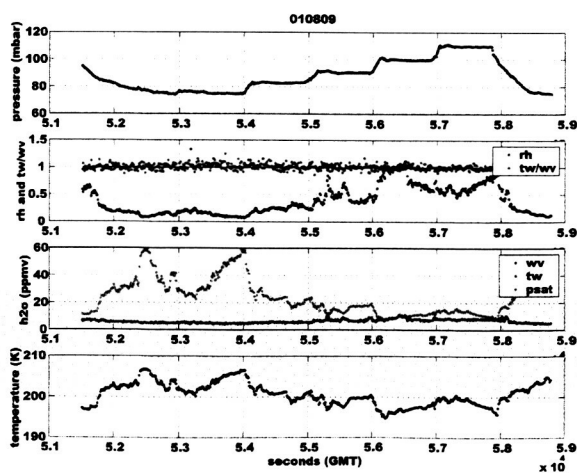


Figure 30: The top panel illustrates the staircase flight profile on August 9, 2001. In the second panel we plot the ratio of total water vapor to water vapor, illustrating the agreement in clear air, over a wide range of conditions in the tropopause region and lower stratosphere, along with the relative humidity, showing that the air is unsaturated. In the third and fourth panels we plot water vapor and temperature, respectively.

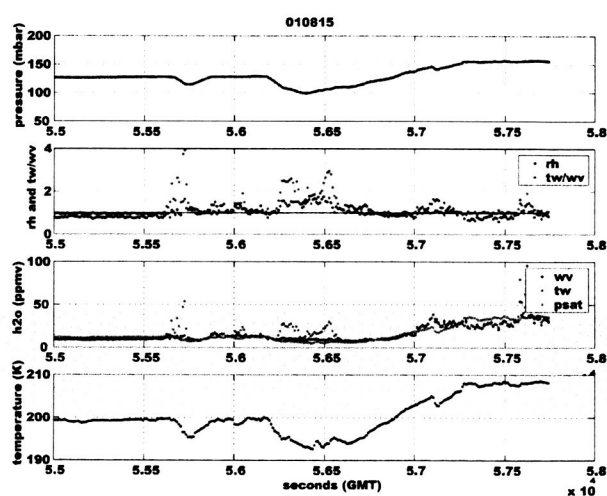


Figure 31: The panels are as in Figure 30, but for August 15, 2001. We illustrate in the second panel the contrast with the data on August 9, 2001, with the deviation of the total water to water vapor ratio in regions of supersaturation, denoting thin cirrus. For these data to be valid requires the evidence (as shown in Figure 30) of agreement between water vapor and total water outside the cloud region.

Absolute accuracy to $\pm 5\%$ is a critical performance criteria for water vapor measurements. We take advantage of the abundance of clouds sampled during flights that facilitate repeated in-flight validation of the total water calibration. This approach takes advantage of a large enough change in total water mixing ratio to enable a direct measurement of this change by absorption, simultaneously utilizing two path lengths and accordingly accounting for any changes in lamp intensity. Along with the laboratory calibrations carried out in the field during the mission, these in-flight comparisons confirm the quoted accuracy of the total water instrument. Figure 32 shows two representative examples of in-flight absorption measurements taken during the CRYSTAL-FACE campaign. The measurement of water vapor by absorption in evaporated clouds is slightly higher than by fluorescence. This slight discrepancy, although within the error bars of the measurements, is still under investigation.

The opportunity was provided during CRYSTAL-FACE to intercompare the total water instrument with two others. One, the ALIAS instrument, was modified to measure total water for the first time using an isokinetic inlet and detection by multipass infrared absorption. The other, the Colorado University total water instrument, measured total water vapor using a sensitivity enhancing anisokinetic inlet with single pass infrared absorption for detection. Ultimately, the first question is how well do these instruments compare in clear air. The Colorado University instrument does not report clear air measurements, so we cannot intercompare it with water vapor measurements in clear air.

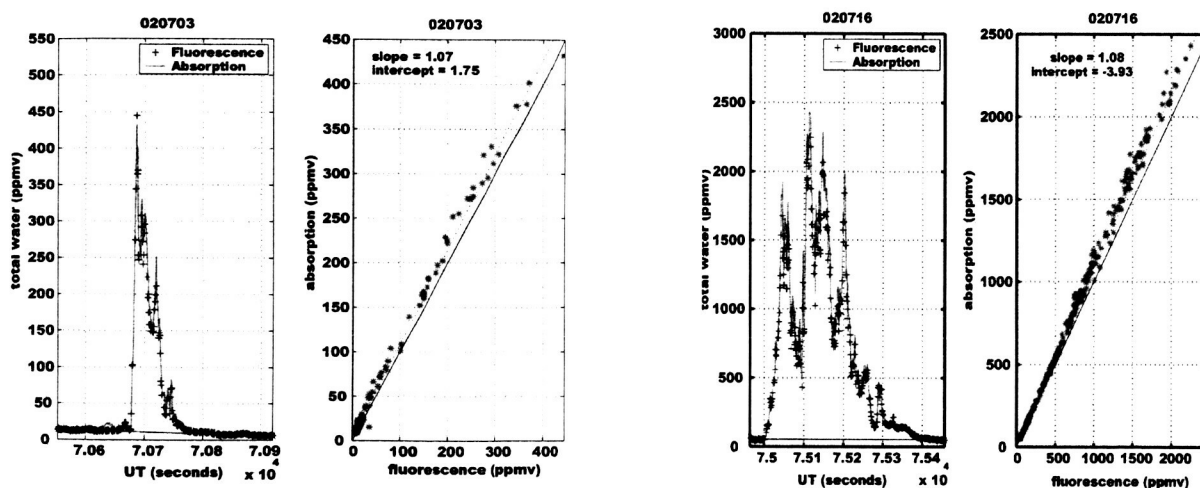


Figure 32: Intercomparison between water vapor measured by absorption and fluorescence during the July 3, 2002, and July 16, 2002, flights.

In Figure 33 we compare water measurements for the two Harvard instruments, JPL water vapor, and ALIAS total water. The left panel is for the flight of July 9, 2002, and the right panel for July 11, 2002, both of which show the reproducible agreement between the two water vapor measurements and the Harvard total water vapor measurements in clear air. The clear difference between those measurements and the ALIAS measurement of water vapor is similar for the two flights and indicates that there are significant systematic errors impacting the latter instrument.

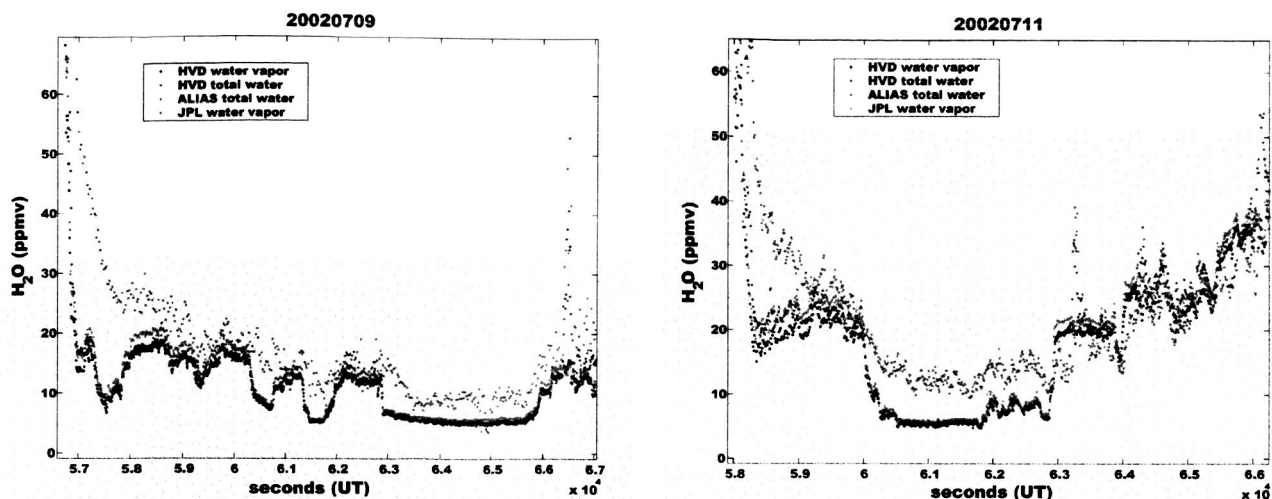


Figure 33: Harvard water vapor, JPL water vapor, Harvard total water, and ALIAS total water for the July 9, 2002, and July 11, 2002, flights during CRYSTAL-FACE. The ALIAS data, plotted in green, exhibits systematic differences with the other measurements.

This illustration of very good agreement between the Harvard photofragment fluorescence instruments and the JPL infrared diode laser absorption hygrometer does not reveal the laboratory calibration effort that was required prior to reporting measured water vapor mixing ratios for CRYSTAL-FACE.

A Laboratory Intercomparison of the Harvard University Lyman- α and JPL Tunable Diode Laser Hygrometers

Preliminary analysis of water vapor measurements made by the Harvard photofragment fluorescence and JPL tunable diode laser absorption hygrometers during the CRYSTAL-FACE campaign in the summer of 2002 indicated disagreements well beyond those exhibited by similar instruments during the POLARIS and SOLVE campaigns. The critical importance of resolving this difference was highlighted during the mission when relative humidity measurements resulting from using Harvard water vapor yielded values of 1.6 in clear air and up to 1.8 in clouds, and 1.3 in a contrail. Similar high supersaturations were seen in the tropical tropopause layer during summer 2001 over Costa Rica. The scientific implications of humidity measurements would be significantly different (and maybe less controversial) when using JPL water vapor measurements that were 25–35% lower than Harvard's. For this reason a laboratory intercomparison of the two instruments was planned for after the mission. This plan could begin to satisfy a number of goals relevant to long-term accuracy issues for water vapor instrumentation, two of which are:

1. To consider these laboratory calibrations as a first step toward the establishment of a long-term plan to maximize the accuracy and precision of *in situ* water vapor instruments.
2. As part of that plan, develop a protocol for calibrations in the field that establishes and/or validates instrument agreement on the ground during a mission.

Intercomparisons between the Harvard Lyman- α hygrometer and the JPL TDL absorption hygrometer typically showed agreement of 5% or better in the stratosphere during both the POLARIS and SOLVE missions. The measurements diverged somewhat with increasing pressure in the tropopause region and below, as described by Hintsa *et al.* (1999). Based on preliminary calibrations the data archived in the field during the CRYSTAL-FACE campaign exhibited a 25–35% difference between the Harvard and JPL water instruments with

Harvard measuring higher and the largest disagreement occurring for ambient pressures below 130 mbar. Because of the previous excellent agreement of the two instruments, we suspected that the differences manifested in flight most likely result from laboratory calibration errors. A laser failure during the May 2002 WB-57 test flights required a new laser and completely new calibration in June 2002, prior to the field mission. The new laser was more temperature-sensitive than the original laser, and overheated in the JPL laboratory calibrations, leading to different performance characteristics on the ground than in flight. Taking these temperature effects into account improved the agreement between the two instruments significantly and the laboratory data taken at Harvard after the mission helped confirm the revised JPL calibration data. Figure 34 compares the Harvard and JPL water vapor measurements during CF using the JPL pre- and post-flight calibration data.

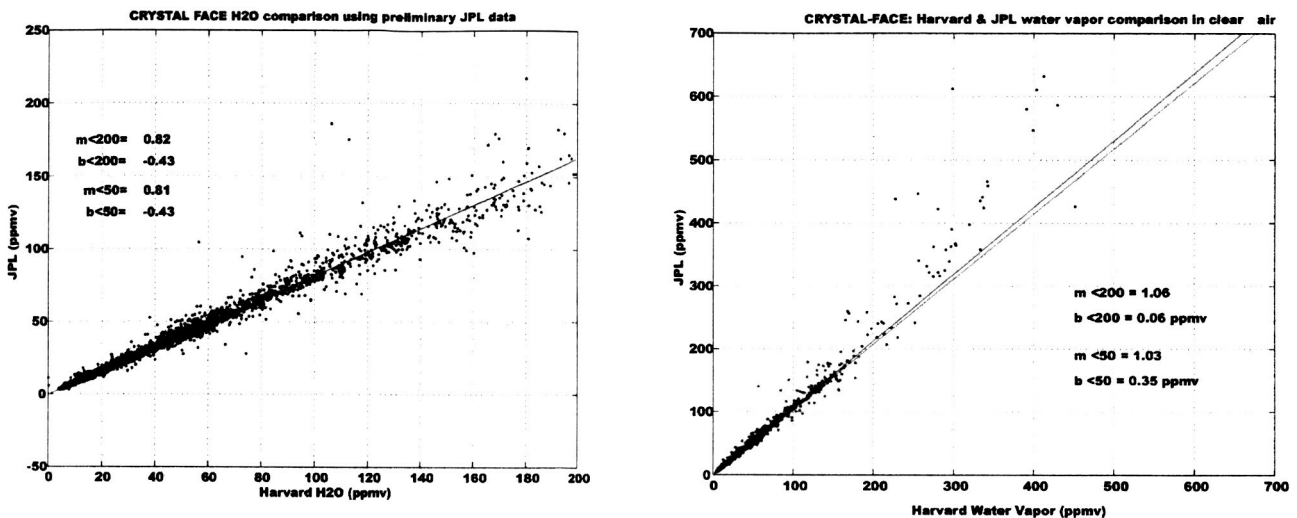


Figure 34: The left panel shows the intercomparison between Harvard and JPL water using JPL preliminary calibration data. The right panel shows the same intercomparison with JPL mixing ratios derived using JPL revised calibration data consistent with calibration data at Harvard University. Fit to the data is shown for data less than 200 and 50 ppmv, respectively.

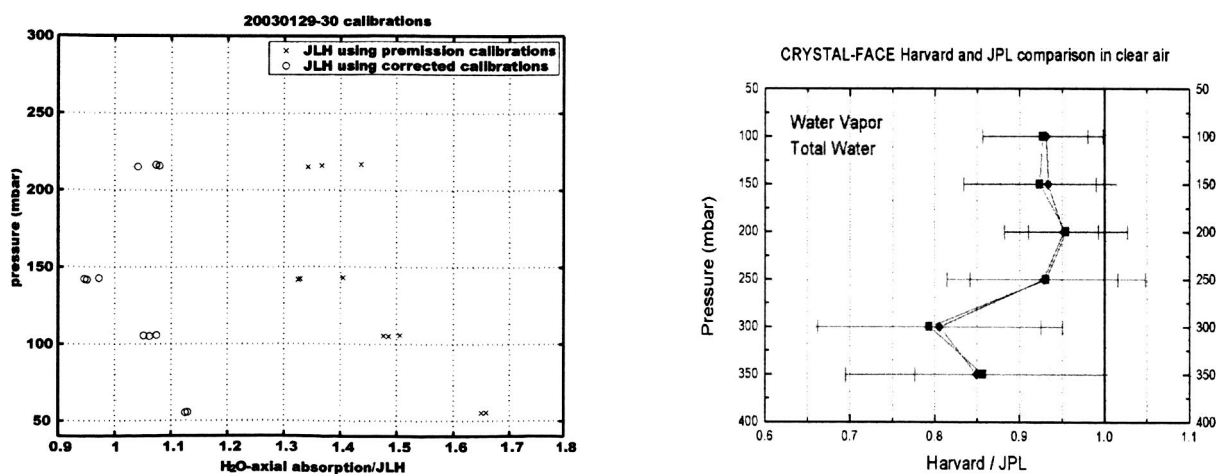


Figure 35: The left panel shows the pressure-dependent plot of the ratio of water vapor measured by absorption during laboratory calibrations *versus* that measured by the JPL hygrometer using both the JPL preflight (x's) and post-flight (o's) calibration data. The right panel shows a plot of the ratio of Harvard water vapor and total water *versus* JPL water vapor binned by pressure.

The left panel of Figure 35 shows a comparison of water vapor measured by absorption in the calibration system *versus* that measured by the JPL hygrometer using both the pre-flight and post-flight calibration data. We see much improvement using the JPL post-flight calibration data. Nevertheless, as shown in the right panel of Figure 35, there are still inconsistencies that have to be checked with further more extensive and careful intercomparisons, both in the laboratory and during field missions.

14. The implications of stratospheric hydration events observed during a mini mission to Costa Rica in August 2001

The CWVCS mission to Costa Rica during August 2001 was organized as a highly cost-effective mini-mission to gather as much data in the Tropopause Transition Layer (TTL) as possible during a period constrained by the availability of low-cost military transportation and limited flight hours. The mission began on August 4, 2001, with a ferry flight from Houston TX to San Jose, Costa Rica, and ended with a return ferry flight on August 18, 2001. During the two-week period in San Jose there were a total of five flights, typically of about six hours duration. Based on regional meteorology, the scientific goals for each flight, and the robustness of the WB57, there were a total of ~ 25 profiles from about 360 K to above 420 K taken during the mission. These profiles were sampled in regions with local conditions ranging from clear sky to heavy convective activity. While the instrument array here is limited, this does represent the first time since the STEP mission that simultaneous measurements of water vapor, total water, and ozone have been made in the TTL, and the first time with a total water instrument using an isokinetic inlet. The critical addition of total water allows for the unambiguous determination of the ice water content of clouds in the TTL, quantifying condensation (but not dehydration). The data presented here utilize measurements of water vapor, total water, ozone, and ambient temperature and pressure, with the focus on two flights, August 9 and 15, 2001, during which a series of profiles through the TTL were measured in varying conditions. We use these two flights because of the very different upper tropospheric temperatures and the resulting difference in the character of the data.

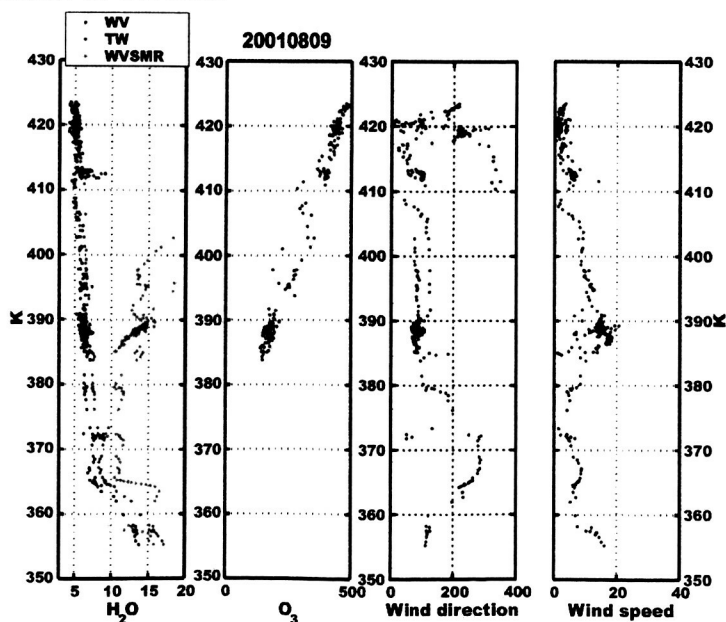


Figure 36: Example of ascent through the TTL on August 9, 2001. The first panel plots water vapor, total water, and saturation mixing ratio. The second panel is a plot of ozone increase in ozone. The third and fourth panels show wind direction and speed.

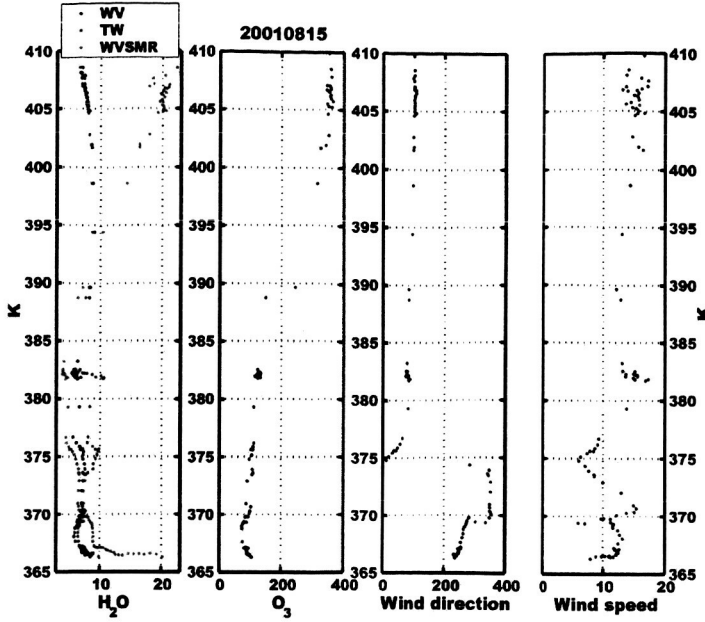


Figure 37: This figure shows the same profiles as Figure 36 for a transect through the TTL on August 15, 2001.

We focus first on the top left quadrant of Figure 36, where at about 412 K both water vapor and total water show a spike of more than 3 ppmv. This water vapor perturbation in the stratosphere, confirmed by two independent measurements, is not accompanied by any measurable change in ozone, nor a significant change in wind direction or speed. At this potential temperature it is no surprise that the air is unsaturated. In principle, the source of this “wet” air could either be air that has slowly advected into the stratosphere that has never seen cold temperatures, or air that was convectively transported into the stratosphere where the particles evaporated. It is difficult to understand how air could slowly rise to that potential temperature surface with a significant water enhancement that is limited in vertical extent. If we arbitrarily use the 390 K surface as the average tropical tropopause, then the air, assuming an average ascent rate of 0.5 K/day, would have been in the stratosphere for about 45 days and the water vapor would have been homogenized. The fact that ozone is nominally unperturbed suggests that if the feature was convectively transported into the stratosphere, the air was in the stratosphere long enough for the ozone to have homogenized, but not long enough for water to be totally homogenized. It would also be consistent with the localized nature of the observation. One can try to calculate the maximum water that can be injected in a convective event with characteristically low ozone, and result in an air mass 3 ppmv higher than expected with virtually no change in ozone. In this case, we assume a simple mixing model in which the convected tropospheric air has 50 ppbv ozone and an unknown amount of water (vapor or ice). With a measured value of ozone of 300 ppbv and, for example, water vapor of 9 ppmv, we assume normal stratospheric air would have 6 ppmv water vapor and 310 ppbv ozone. For ozone, we can’t really see any perturbation from the stratospheric value so we just choose an arbitrary difference to allow the calculation to proceed. We now have for ozone:

$$\text{fr}(\text{O}_3)_{\text{conv}} * (\text{O}_3)_{\text{conv}} + \text{fr}(\text{O}_3)_{\text{strat}} * (\text{O}_3)_{\text{strat}} = (\text{O}_3)_{\text{meas}} \quad (1)$$

where $\text{fr}(\text{O}_3)$ represents the fraction of O_3 . We use 50 ppbv for $(\text{O}_3)_{\text{conv}}$, 310 ppbv for $(\text{O}_3)_{\text{strat}}$, and 300 ppbv for $(\text{O}_3)_{\text{meas}}$. Assuming $\text{fr}(\text{O}_3)_{\text{conv}} + \text{fr}(\text{O}_3)_{\text{strat}} = 1$, we get that $\text{fr}(\text{O}_3)_{\text{conv}} = 0.0385$. Then, using a similar equation for water

$$\text{fr}(\text{H}_2\text{O})_{\text{conv}} * (\text{H}_2\text{O})_{\text{conv}} + \text{fr}(\text{H}_2\text{O})_{\text{strat}} * (\text{H}_2\text{O})_{\text{strat}} = (\text{H}_2\text{O})_{\text{meas}} \quad (2)$$

where we assume $(\text{H}_2\text{O})_{\text{strat}}$ is 6 ppmv, $(\text{H}_2\text{O})_{\text{meas}}$ is 9 ppmv, we determine that $(\text{H}_2\text{O})_{\text{conv}}$ is 204 ppmv. Thus an air mass would have to ascend into the stratosphere up to 412 K maintaining 204 ppmv water vapor. If this air mass were not convectively hydrated, then assuming dehydration to supersaturation at 100 mbar, this would correspond to an unrealistic minimum temperature of 218 K along the back trajectory of the air parcel.

The other example is exhibited in the first quadrant of the right-hand panel where the water and total water data indicate the presence of a cloud with 4–7 ppmv ice water content. The profile exhibited by the total water would seem to be too high to be consistent with a cirrus cloud formed in situ, and we therefore believe it is cirrus blowoff from a convective system. This is of course very important because of the extreme supersaturation observed in the cloud. Both the water vapor ($\pm 5\%$) and temperature (± 0.5 K) accuracies provide the necessary confidence in this measurement. While the implications of this measurement might be even more profound if this cloud were formed in situ, this observation is evidence that the nucleation processes in optically thin cirrus near the tropical tropopause (we postulate whether formed in situ or from convective blowoff) do not reduce the relative humidity to near 1. Accordingly, tropopause cold trap temperatures need to be significantly colder than previously thought to adequately dehydrate the stratosphere. We also focus on the profile above the cloud where water vapor gradually increases from about 6 to 9 ppmv. The ozone profile indicate a fairly sharp discontinuity at cloud top, providing strong evidence that that increase in water vapor is not related to the cloud below. Based on the observation of other instances of convection into the lower stratosphere, we also attribute this rise in water to convective hydration. The air transitions in this region from slightly supersaturated to significantly undersaturated with increasing potential temperature. Nevertheless, these observations suggest that convection serves as a significant source of moisture to the tropical stratosphere in summer. However, without additional tracers, one cannot rule out that the humidity of this air mass was set by the minimum temperature it experienced as it ascended into the stratosphere.

15. Quantifying isentropic transport in the middleworld during CRYSTAL-FACE using tracer-tracer correlations and a simple mixing model

We use high resolution, *in situ* measurements of H_2O , O_3 , CO_2 , CO and NO_y aboard NASA's WB-57 made during the CRYSTAL-FACE campaign during July 2002 and a simple mixing model to study the dynamics of the middleworld in the subtropics during this time of the year. The goal of this model is to quantify the various transport mechanisms that regulate the mixing ratios of water vapor and O_3 in the Upper Troposphere/Lower Stratosphere.

Figure 38 shows a schematic of four possible transport pathways into the middleworld as denoted by the thin solid arrows: (1) diabatic descent from the tropical stratosphere; (2) quasi-isentropic transport equatorward from higher northern latitudes; (3) quasi-isentropic transport poleward from the Upper Tropical Troposphere (UTT); and (4) direct convective input from below. We first model the dynamics in this region without the convective component (pathway 4). We create profiles for tracers in each source region using ozonesonde data and *in situ* measurements from previous aircraft

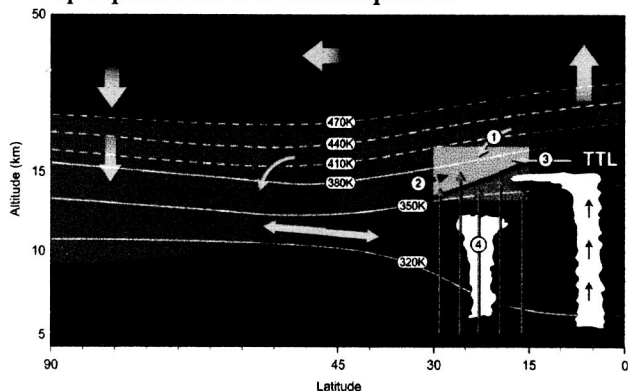


Figure 38: A plot of isentropes in the northern hemisphere as a function of latitude and altitude with details as described in the text.

campaigns.

Figure 39 shows a comparison of profiles of ozone, carbon dioxide, and water vapor measured on July 3, 2002, with profiles from the different source regions (dots), color-coded according to the different source regions, where the stratospheric source regions are sorted by latitude. In this way the stratospheric air can range from being very young (20°N), having recently entered the tropical stratosphere, to much older, containing a significant fraction of air that has been in the stratosphere for a few years (58°N). The UTT air is distinguished by the much higher water vapor content because the air has not passed through the tropical tropopause where it would have been more significantly dehydrated.

Finally, the linear combinations of the UTT profiles and the different stratospheric source profiles are plotted (circles) where the fraction of stratospheric air decreases linearly from 100% at 400 K to 0% at 340 K. the general agreement for these three tracers gives us confidence that a simple mixing model can be successful.

We now use the same source region profiles and a least squares fitting routine that simultaneously evaluates the fit to the five tracers independently for each data point to best match the measured composition of air parcels sampled. The output of the model gives us the mixing fraction for each transport pathway. Figure 40 shows an example of modeled profiles for the July 3, 2002, flight, illustrating the generally good agreement and, at least for this flight, no contribution from pathway 1 to the air in the middleworld.

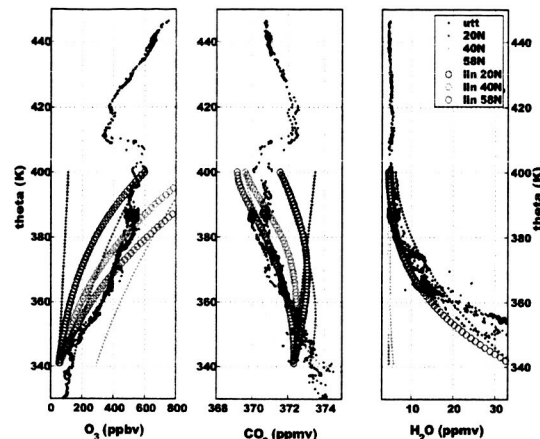


Figure 39: Measured and simulated profiles of O_3 , CO_2 and water vapor as described in the text.

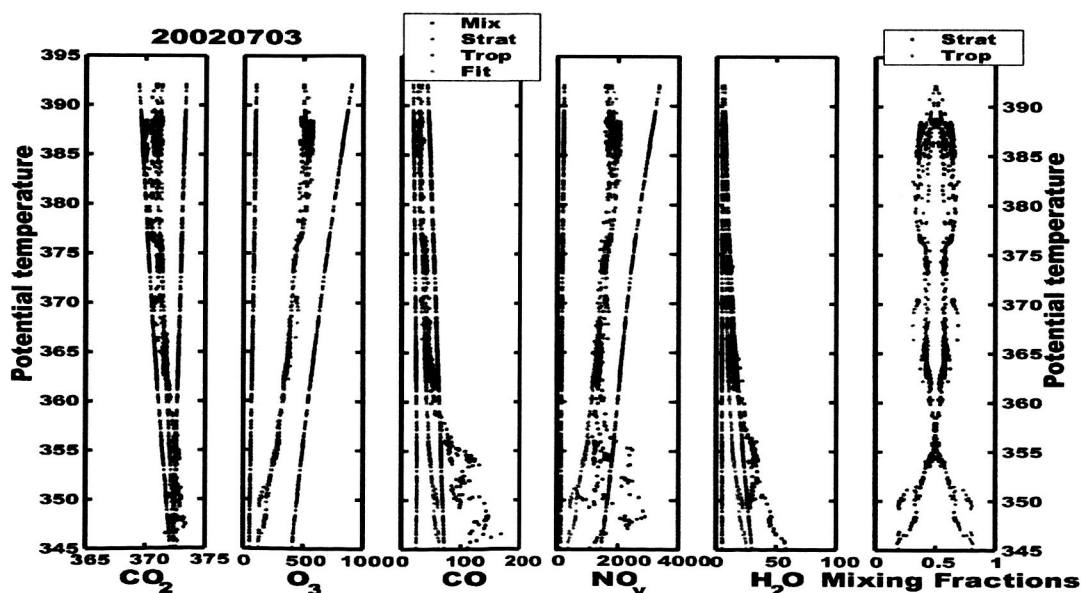


Figure 40: Comparison of measured and modeled tracer profiles for the 20020703 flight. Each of the first five panels contains the source region, measured and modeled profiles. The right-hand panel shows the calculated fractions of stratospheric and tropospheric air. The poor agreement below 360 is clearly caused by convective influence.

The model will be expanded to allow the following:

1. Exploration of the degree to which convection has influenced the middleworld for these data. The upper tropospheric and middleworld air sampled during CRYSTAL-FACE was influenced both by local convection and northern latitude convection. How well can we identify and distinguish between the contribution of these two sources?
2. Extension of the model to flight segments that extend deeper into the troposphere that are influenced by convection, and finally into regions that contain cirrus clouds.
3. Investigation of the choice of and sensitivity to the UTT source profiles. Because water vapor in the UTT is most variable, its uncertainty on the one hand is by far the greatest and on the other hand its contribution in the middleworld is most important. Accordingly, will the model allow us to quantify the difference between water vapor in the UTT component of the middleworld air sampled early in the month of July *versus* later in the month, when back trajectories indicated different source regions?
4. Determination of the northernmost extent of the source region for midlatitude air based on the location of the subtropical jet. Summertime middleworld measurements during POLARIS as compared to during STRAT indicate that the age spectra of lower stratospheric air at 40°N and 60°N are very different.

16. Observations of hydration in the upper troposphere by convective events: Case studies during CRYSTAL-FACE

Understanding the impact of Upper Troposphere (UT) cirrus is important both for their role in regulating the climate through radiative processes and because of their influence on the water vapor and chemical makeup of the UT (Potter *et al.*, 1995; Yin *et al.* 2002). One of the predominant ways of forming cirrus is from the outflow of convective systems (Massie *et al.*, 2002). Cirrus formed by convection bring saturated air and ice nuclei into the UT. For weak convective events residence times of the cirrus are short and therefore the amount of mixing with ambient air and the total amount of water vapor deposited in the UT are small. Most of the water brought up by this convection is removed by sedimentation and evaporates in the middle troposphere (< 12 km). For strong convective events the residence times of the cirrus outflow are long enough for significant mixing to occur. If the air is supersaturated the aerosols and ice particles injected by the cirrus accumulate water and bring the air down to saturation. If the air is not saturated then the evaporation of ice occurs and the air is brought up to saturation.

During the CRYSTAL-FACE mission that took place during July 2002 out of Key West, Florida air was sampled in and around cirrus outflow. One of the purposes of these flights was to understand the role of outflow cirrus in controlling UT water vapor. However, there were very few profiles made downstream of convective systems and there were no instances where a cirrus cloud was sampled through dissipation. We therefore rely on convective signatures in order to understand the role of cirrus in setting the water vapor in the midlatitude UT during July. These signatures result from the fact that convection along with water vapor also brings trace gases from the boundary layer up into the UT. The concentration of these tracers are different from their UT values and therefore allow us to look at the results of convection without having to actually follow a specific cloud.

Two types of hydration were observed in clear air around cirrus. The first type is caused when ice particles convect into the UT mix with undersaturated air and evaporate. The observed increase in water vapor is accompanied by tracer mixing ratios consistent with convective air rather than ambient UT air. During CRYSTAL-FACE this type of hydration was observed mostly above the main cirrus cloud and usually just above the local tropopause where the air was

undersaturated. An example of this is shown in Figure 41, where an increase in water vapor (left panel) is observed just above the local tropopause, which lies between 365 and 370 K. The air mass sampled had recently passed through a region of very strong convection. The increase in water vapor, shown in cyan, is correlated with lower ozone (third panel) and increased carbon monoxide (fourth panel), both of which indicate convective air.

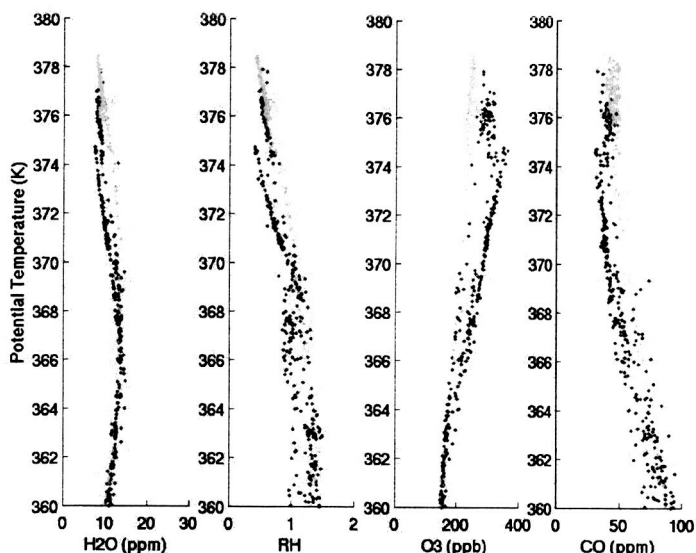


Figure 41: Hydration event observed above the local tropopause on July 13, 2002. The first panel shows the water vapor mixing ratio measured by the WB-57. Two profiles are shown, with the one in cyan showing an increase in water vapor. Also shown are the relative humidity (second panel), ozone mixing ratio (third panel) and carbon monoxide mixing ratio (fourth panel). The green points correspond to the profile with the increased water vapor.

Another hydration event observed in the lower stratosphere is shown in Figure 42. Using back trajectories and data on the chemical makeup of the particles contained in the air this hydration came from strong convective events associated with forest fires in Canada and the northern US. The convective signature for this event is very different from that of local convection, which was shown in Figure 41. The change in water vapor and other tracers is at one level and does not form a mixing line back to the local tropopause. In addition the amount of ozone is much larger, indicating older air, and the CO is greater than a hundred ppm, indicating air originating from the burning of biomass. Both of these events show evidence that strong convection can penetrate into the lower stratosphere. The hydration from these events is accompanied by changes in tracer mixing ratios which leave a signature as to the convective origin of the water vapor.

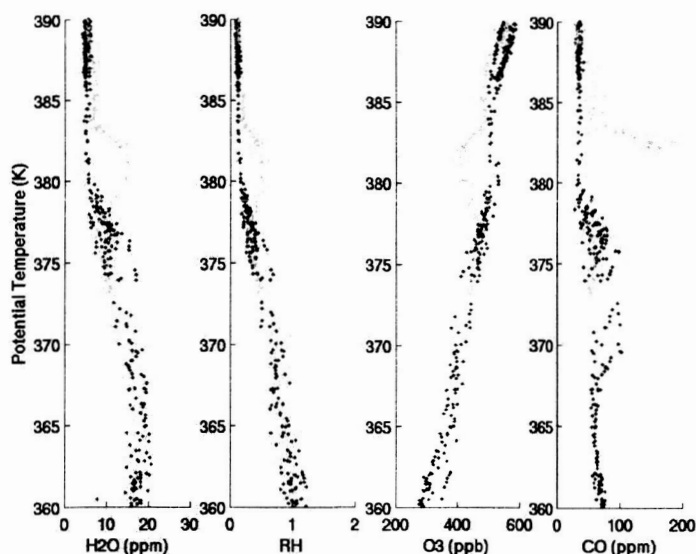


Figure 42: Hydration event observed in the stratosphere on July 7, 2002. The first panel shows the water vapor mixing ratio measured by the WB-57. Two profiles are shown, with the one in cyan showing an increase in water vapor. Back trajectories show that this air came from region with intense forest fires. Also shown are the relative humidity (second panel), ozone mixing ratio (third panel) and carbon monoxide mixing ratio (forth panel). The green points correspond to the profile with the increased water vapor.

The second type of hydration event observed during CRYSTAL-FACE is caused by the evaporation of ice particles as they sediment out from the cirrus into undersaturated air in the middle troposphere. This type of hydration is not accompanied by changes in tracer mixing ratios, except for those tracers that are absorbed onto the ice particles, such as nitric acid. This type of hydration mainly occurred below 345 K.

In summary, the convection observed over southern Florida in July brought moist air up to the UT. However, most of this water vapor was removed by ice sedimentation followed by evaporation below 350 K. This was due to the fact that during CRYSTAL-FACE the UT was mainly saturated and sometimes supersaturated. Therefore, hydration at the cirrus level is not expected. Because the aircraft was not able to follow the cirrus through its dissipation, it is not clear to what extent cirrus outflow from convection regulates the saturation level of the UT. It will certainly depend on the residence time of the cirrus, which in turn depends on the aerosol type and ice nuclei size distribution as brought up by convection and saturation level of the ambient air. The amount of water vapor deposited in the UT as measured by the WB-57 appears to be small and mostly at or above the local tropopause where the air is undersaturated. However, if convective penetration of the tropopause occurs consistently, it may be an important mechanism for hydrating the lower stratosphere especially in areas with strong convective systems.

17. Studying the evolution of cirrus clouds during CRYSTAL-FACE: A mixing model using tracer-tracer correlations

Cirrus clouds play an important role in regulating the radiative budget and relative humidity of the upper troposphere (UT). In order to understand how chemical changes in the boundary layer will affect the climate system it is necessary to understand how changes in convective intensity and chemical makeup will affect the lifetime and growth of cirrus clouds. To do this we need to understand what physical and microphysical conditions determine the evolution of total water in cirrus anvils (Liu *et al.*, 2003; Twohy, *et al.*, 2002). In order for measurements of individual cirrus clouds to provide useful information concerning the processes that control cirrus cloud lifetime and dehydration efficiency we need to place those measurements in the context of the evolution of the cirrus cloud. Many of the measured quantities, such as saturation level, particle size distribution, and total water, are time and mixing

dependent and therefore require knowledge on mixing rates between the cloud and the surrounding air. For outflow cirrus from convective systems we are aided by the fact that the concentration of certain trace gases (CO_2 , CO , O_3 , formaldehyde, etc.) in the boundary layer can be very different from their concentrations in the UT. A simple mixing model has been developed to study the mixing history of cirrus blowoff from convective anvils and the evolution of total water during the lifetime of a convective event.

In our model, convection is viewed as shown in Figure 43.

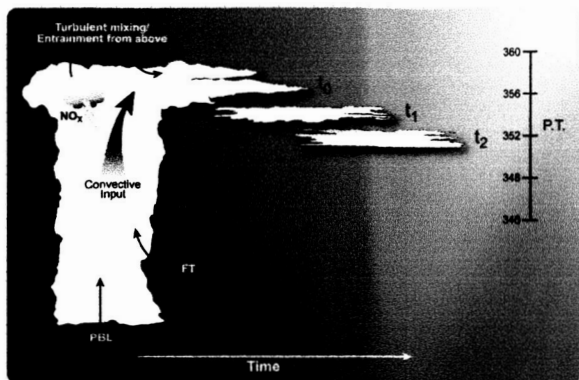


Figure 43: Schematic of convective mixing in the UT. t_0 : Initially a cumulus cloud forms, which entrains air and moisture from the planetary boundary layer (PBL) and the lower free troposphere (FT). In the cloud lightning can generate large concentrations of NO_x , thus elevating NO_y above its FT value. This mixture is convected upwards until it reaches the top of the troposphere. The cloud starts to spread out forming an anvil and causing turbulent mixing which entrains air from above the cloud top. t_1 : The cirrus blowoff from this anvil slowly sinks and mixes with ambient air. t_2 : The cirrus continues to sink and mix with ambient air eventually dissipating through sedimentation and evaporation.

Initially, a cumulus cloud forms and entrains air and moisture from both the planetary boundary layer (PBL) and the free troposphere (FT). This mixture is convected upwards until it reaches its detrainment level at the top of the troposphere. The cloud starts to spread out forming an anvil and causing turbulent mixing which entrains air from above the cloud top. The cirrus blowoff from this anvil mixes with ambient air as it spreads, eventually dissipating through sedimentation and evaporation. In order to calculate the amount of mixing that has occurred within the cirrus blowoff it is necessary to know the mixing ratios of tracers being detrained from the convection and also the vertical profile of the tracers before the ambient air was mixed with convective air. While we do not have tracer measurements in the absence of convection, air furthest away from the cloud will have undergone the least amount of mixing with the cloud air. In the case of data from the CRYSTAL-FACE mission, we use air that is at least 15 km from the cloud. For the model we use the tracers O_3 , CO , CO_2 , and NO_y . Their mixing ratios for the convective air are obtained from boundary layer data near the cloud base in the case of O_3 and the STILT model (Gerbig *et al.*, 2002) in the case of CO and CO_2 . NO_y is based on passes through the thickest parts of the anvil since most of the NO_y is generated in the cloud by lightning. An example of these profiles is shown in Figure 44 for the flight of July 16, 2002. For each of the four tracers shown, the blue line represents the pre-convective profile, the black line represents the mixing ratio of the tracer being detrained from convection, the red dots are measurements made in the cloud, and the cyan dots are measurements made in clear air around the cloud.

We hypothesize that the concentration of tracers sampled by the aircraft will be a linear combination of the tracer mixing ratios in the convective air and the ambient UT air. The amount of mixing that has occurred between the convective air (boundary layer and free troposphere) and ambient air is calculated by using a least squares fitting algorithm to minimize the equation

$$C^*x - P = 0, \quad (1)$$

where C is a matrix whose columns contain the tracer mixing ratios of the convective air and the ambient air binned into 2 K potential temperature levels, x is a vector containing the fractions of

air from each component to be determined, and P is a vector containing the mixing ratio of the tracers as measured by the WB-57 in the UT.

The results from the model for a segment of the flight of July 16, 2002, in which the WB-57 made several passes through the same cirrus cloud are plotted in Figure 45. The top plot shows the potential temperature (PT) of the air sampled. The middle plot shows the concentration of ice sampled as measured by the Harvard Total Water instrument. Finally the bottom plot shows the output from the model. The components of the air are plotted as fractions versus time. The fraction of convective air is shown in dark purple and the fraction of ambient air is color coded by PT as shown in the legend of Figure 45. The initial pass through the cirrus outflow shows a very sharp cutoff between the cloud and clear air. The cirrus at this point is mainly air from convection as indicated by the fraction of convective air approaching one. As expected subsequent passes through the cirrus show progressively more mixing and therefore more ambient air. By plotting the mixing history of the cirrus against particle size distribution data and total water concentrations in conjunction with remote sensing data from radar and lidar, we will be able to watch the evolution of a cirrus cloud throughout its lifetime. Differences between different cirrus clouds can then be related back to differences in the microphysical and microdynamical properties of the convective system.

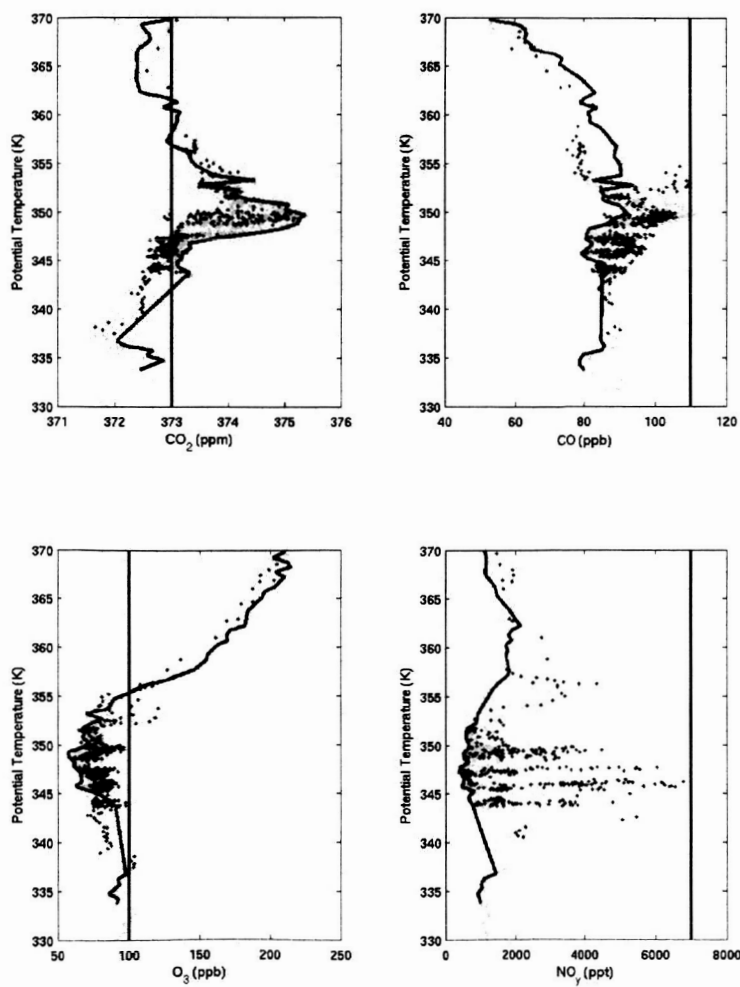


Figure 44: Ambient and convective profiles from the flight of July 16, 2002, for CO_2 , CO, O_3 , and NO_y used in the model. The blue line represents the ambient profile. While we do not have measurements of the air parcel in the absence of convection, air far removed from the cloud will have undergone the least amount of mixing with the cloud air. In this case we use air that is at least 15 km from the cloud. The black line represents the value of the convective input (CO_2 and CO are calculated based on the STILT model (Gerbig *et al.*, 2002); O_3 is based on tracer-tracer correlations near the surface; and NO_y is based on passes through the thickest parts of the anvil). The cyan dots are measurements made in clear air around the cloud and the red dots are measurements made in the cloud.

In order to deploy this approach for studying cirrus clouds measurements must be made that sample the air that is entrained from the boundary layer and the air that is detrained from the convective system. Flight trajectories should include legs that go horizontally along the cirrus outflow as well as vertical profiles (spirals) through the cirrus. The horizontal legs should extend far enough past the cloud boundary as to get a sample of air unperturbed by convection (both upwind and downwind). The vertical profiles should also include sampling of air above and below the cirrus. The transits should continue throughout the lifetime of the cirrus and include a vertical profile of the remaining air once the cirrus has dissipated (assuming the lifetime of the cirrus is not longer than the flight time of the aircraft). The context for the *in situ* measurements in terms of the a 3-D structure of the cloud will be created using radar/lidar aboard a high-altitude aircraft (ER-2) whose flight plan would be coordinated with the WB-57.

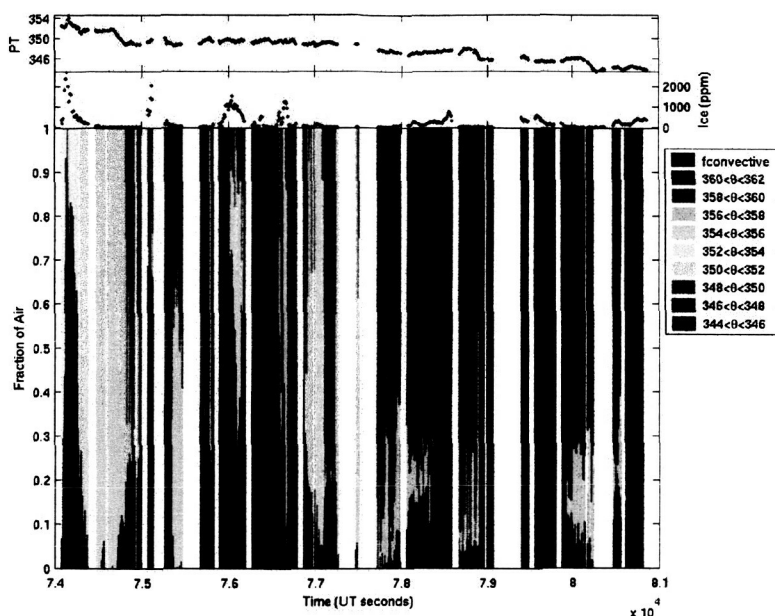


Figure 45: Top plot shows the potential temperature of the air parcel versus time in UT seconds. The middle plot shows ice measured using the Harvard total water and water vapor instruments. The bottom plot shows the fractions of different air that make up each air parcel sampled by the WB-57 according to the model. The dark blue represents the fraction of convective air in the parcel, the lighter blue through brown represents the fraction of air from different potential temperature levels as shown in the legend.

18. Equatorward isentropic transport of northern midlatitude stratospheric air observed over Florida during CRYSTAL FACE

Understanding the coupling between chemistry and dynamics in the atmosphere is crucial for predicting future changes in the global climate system and their impact on human health. Observations in the middleworld, the region in the stratosphere bounded from below by the local tropopause and from above by the tropical tropopause which is typically between the 380 K and 390 K isentropic surfaces, have shown seasonal changes in both chemical composition and dynamics. For instance, ozonesonde data show a decreasing trend of ozone in northern midlatitudes during the last decade with the maximum loss taking place in the middleworld during the springtime (Logan *et al.*, 1999). Satellite observations show increasing trends of water vapor in the middleworld, which could cause an increase in both polar and midlatitude ozone loss by providing the surface (e.g., polar stratospheric clouds, cirrus clouds) where catalytic reactions that destroy ozone take place. In addition to the observed chemical changes, the middleworld could serve as a gateway for aircraft emissions to reach the troposphere and the Tropical Tropopause Layer, and impact both the local and the global chemical environment. Thus, it is important to understand what controls the seasonal changes of the chemical composition and the transport mechanisms of air in the middleworld.

Two recent aircraft campaigns have allowed us to perform *in situ* measurements in the middleworld during different seasons. Results from tracer-tracer correlations using measurements obtained from the ER-2 during the SOLVE campaign in 2000 show a dominant poleward transport of air from the tropical lower stratosphere to the high latitude middleworld during late winter and early spring (Spackman *et al.*, 2005). Tracer measurements obtained aboard the WB-57F during the CRYSTAL FACE (CF) campaign in 2002 show a dominant equatorward transport of air from the high latitude middleworld to the subtropical middleworld during the summertime, instead.

The equatorward transport we observed in the subtropics during summer 2002 is revealed both in the tracer field and in the meteorological field. In terms of tracers, we see evidence of this transport in the ozone and water vapor profiles. Figure 46 shows a comparison of the ozone and water vapor profiles in the tropics and subtropics during two summertime campaigns: STRAT in 1996 and CF in 2002. It can be observed how ozone levels in the middleworld were up to 300 ppbv higher during CF, in particular during the first half of the campaign (cyan points), with corresponding water vapor values higher than those expected coming from the tropical tropopause. These two tracers suggest a strong influence of both high latitude stratospheric air and tropospheric air in the subtropical middleworld.

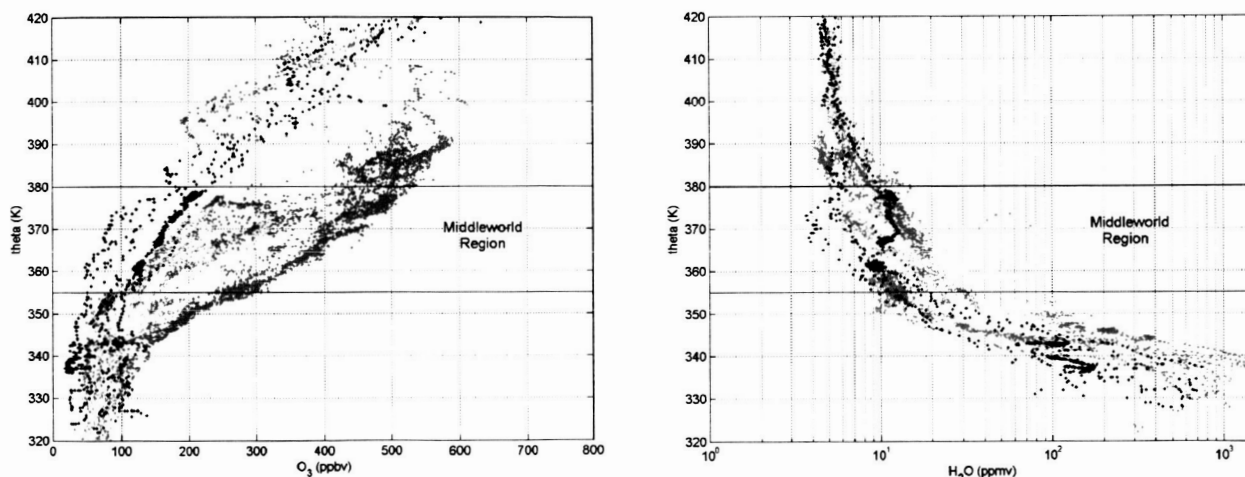


Figure 46: Ozone and water vapor profiles *versus* isentropic surfaces for tropical and subtropical data during the month of July. The cyan points correspond to the first half of the month during CRYSTAL-FACE in 2002, the yellow points correspond to the second half of the month during CRYSTAL-FACE in 2002, and the black points correspond to STRAT in 1996.

The ozone profile in Figure 46 shows a transition from what appears to be older stratospheric air (from high latitude) to younger stratospheric air (from the tropics) (cyan and yellow points, respectively). In order to understand what controls this transition, we focus on one isentropic surface. Figure 47 shows profiles of O_3 , CO_2 and H_2O on the 380 ± 2 K surfaces. We can observe the dominant presence of older stratospheric air (high O_3 and low CO_2) during the first half of the month (red points) and a change to predominant younger stratospheric or convective air (low O_3 and high CO_2) during the second half of the month (cyan points). The H_2O profile does not show a clear change throughout the month; however, it shows evidence of convective intrusion between 381 and 382 K on July 7 and 9.

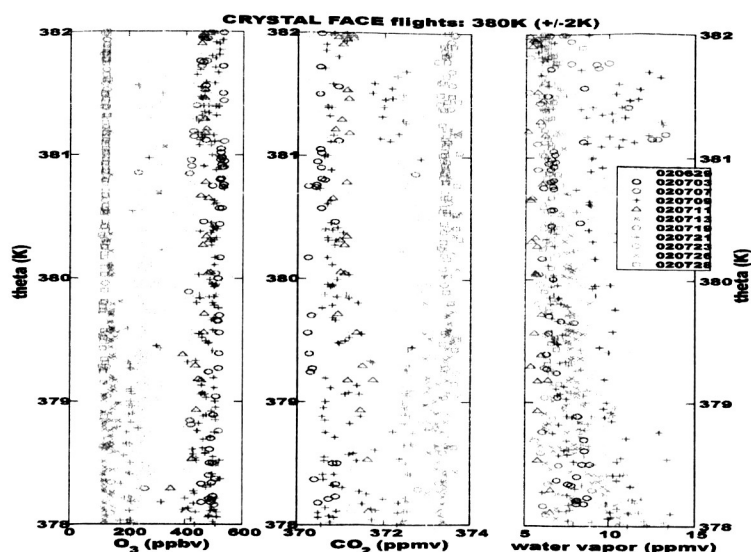


Figure 47: Profiles of O_3 , CO_2 , and H_2O as a function of θ for the 380 ± 2 K isentropes for all flights during the CRYSTAL-FACE campaign in 2002. The yellow points correspond to the ferry flight from Houston, TX ($29^\circ N$) to Key West, FL ($25^\circ N$). The red points correspond to the first half of the month of July. The cyan points correspond to the second half of the month of July.

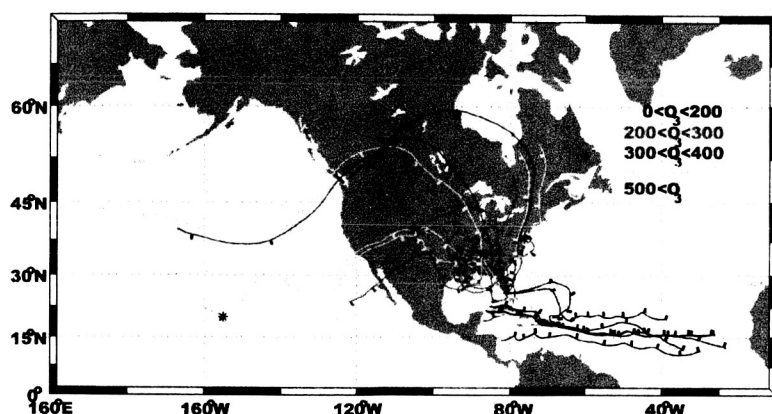


Figure 48: Ten-day isentropic back trajectories on 380 ± 2 K for the CRYSTAL-FACE campaign. The trajectories are color-coded based on the measured ozone mixing ratios in ppbv during CRYSTAL-FACE. The black asterisks correspond to locations of ozonesonde stations.

In terms of meteorological fields, we see a correlation between changes in the chemical signature and changes in dynamics. Figure 48 shows 10-day isentropic back trajectories on the 380 K surface for July 2002 color coded by the measured ozone mixing ratios during CF. The trajectories traveling equatorward towards Florida with ozone mixing ratios higher than 200 ppbv were observed during the first half of the month, whereas the trajectories with less than 200 ppbv of ozone were observed during the second half of the month.

Both observed changes in tracer profiles (Figure 47) and in dynamics (Figure 48) validate the coupling of the two during the CF campaign. Thus, understanding what controls the strength, seasonality, and longitudinal variation of transport mechanisms in the middleworld as well as the chemistry of this region is crucial for assessing future variations of northern midlatitude ozone and the impacts on human health.

19. Direct measurements of OH yields from gas-phase ozone-alkene reactions using an *in situ* LIF instrument

In this study, direct, pressure-dependent measurements of OH yields from gas-phase ozone-alkene reactions are measured, using the ER-2 HO_x instrument to obtain sensitive, accurate, and precise OH concentrations. As in previous studies from this laboratory, steady-state [OH] is measured by laser-induced fluorescence (LIF); here, the accurate LIF calibration allows us to present absolute OH yields for the first time. To calibrate our original LIF system, yields from ozone plus tetramethylethylene (TME) are measured as a function of pressure. The pressure dependence agrees with previous results, so that yield measurements are now of comparable accuracy to those in indirect studies. Prompt, low-pressure yields agree well with 1 atm yields measured over longer timescales, confirming that much of the OH arises from decomposition of stabilized carbonyl oxides. In addition, pressure dependences of yields from the terminal alkenes ethene, isobutene, and isoprene are also measured.

The results from this study indicate the feasibility of using the HO_x instrument for the measurement of OH in the troposphere. Such measurements may be hampered by ozone photolysis within the laser beam; the resultant O(¹D) atom may then abstract a hydrogen from a water or hydrocarbon molecule, generating OH in the detection region. Laser generation of OH is a potential interference in this study as well, as hydrocarbon concentrations were high ($\sim 10^{14}$ molecules/cm³) and ozone concentrations were moderate ($\sim 10^{12}$ molecules/cm³). However, running at high laser pulse repetition rates (10 kHz) and low peak laser power (30–100 nJ/pulse) leads to minimal photolysis of ozone, so that the contribution by laser-generated OH is negligible. At such low power sensitivity still high ($\sim 10^5$ OH/cm³) enough to permit precise yield measurements.

20. BrO measurements in the arctic winter stratosphere

It is well-established that bromine compounds, which enter the atmosphere from a variety of natural and anthropogenic sources, cause stratospheric and tropospheric ozone depletion. Bromine compounds are actually much more efficient at ozone destruction on a per atom basis than are chlorine compounds. Efforts to test the abundance and speciation of bromine in the stratosphere, however, have been particularly hampered by low atmospheric concentrations. An instrument recently designed and built in this laboratory, which is capable of measuring BrO *in situ* in the stratosphere with a higher signal-to-noise ratio than ever previously attained, is described in the section: “ClO and BrO resonance fluorescence, IO laser-induced fluorescence, and ClOOCl, ClONO₂, and BrONO₂ thermal dissociation/atomic resonance scattering instrument”. Bromine data acquired with the Harvard Halogen flight instrument on the SOLVE mission to Kiruna, Sweden, are presented and discussed here.

Prior to the SOLVE mission, the majority of the *in situ* measurements of BrO in the stratosphere had been made onboard the NASA ER-2 aircraft with the Harvard ClO/BrO instrument, a predecessor to the current Harvard Halogen instrument. The basic mode of operation was resonance fluorescence detection of Br atoms generated from chemical titration of BrO with NO. This is the analogous technique to that for ClO. Because the BrO concentrations

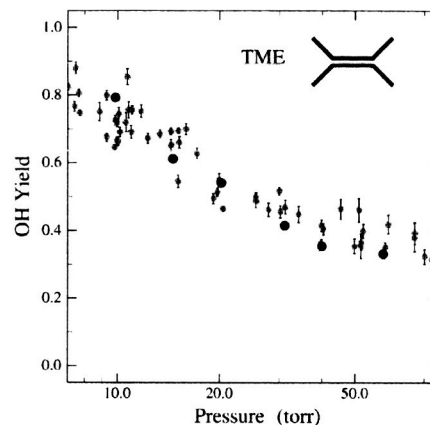


Figure 49: OH yields from the ozonolysis of TME as a function of pressure; black points are from this study, gray points are from our previous study, corrected for calibration errors.

were low, the Br fluorescence signal was weak relative to the background signal, and long averaging times were required. Typically, less than ten BrO measurements were produced for an eight-hour ER-2 flight.

Figure 50 shows sample data from the Harvard ClO/BrO instrument acquired at northern midlatitudes in the wintertime lower stratosphere (Brune *et al.*, 1988). The ClO measurements were made approximately every 35 seconds, while the BrO measurements were only acquired approximately every 40 minutes due to long averaging times. The paucity of data and relatively poor signal-to-noise ratio shown here are typical of all previous *in situ* measurements of BrO.

The redesign of the RF detection axis for bromine prior to SOLVE provides the capability to detect BrO with greater sensitivity, precision, and spatial resolution than in any previous *in situ* ER-2 measurement. Measurements of BrO were successfully made during twelve flights of the SOLVE mission.

Analysis of the BrO data is aided by using ClO as an indicator of the chemically perturbed region inside the polar vortex. Of particular interest

are observations of BrO during the day and at night and relative measurements from inside and outside the vortex. Figure 51 shows ClO and BrO signals for four representative flights of the mission. Inside the Arctic vortex, the BrO signal tends to exhibit the same shape as the ClO signal, i.e., increases or decreases in the observed amounts of BrO and ClO typically occur concurrently during flights inside the vortex. This is particularly poignant in the flights which involve daytime-nighttime transitions, as exhibited on January 20, January 31, and February 2, 2000. For each flight, high levels of ClO and BrO characterize sunlit conditions, while the signals drop to much lower levels in darkness. The 0131 flight is particularly interesting. The ER-2 took off in sunlight, traveled north within the vortex into darkness, then returned south where sunlight was again encountered. The changing levels of ClO and BrO during the flight correlate well. There is a clear diurnal dependence for BrO.

While the BrO signal tends to exhibit the same pattern as that of ClO inside the vortex, this behavior does not hold across the vortex edge. The flight of March 11, 2000, shown in the bottom right panel of Figure 51, began inside the Arctic vortex, crossed the vortex edge and continued outside for several hours, then reentered the vortex for approximately the final three hours of the flight. The region outside the vortex is clearly indicated by the precipitous drop in ClO concentration. The BrO signal, however, remains relatively unchanged throughout the flight. These observations indicate that while ClO levels are highly dependent on whether the measurement is taken inside or outside of the vortex, BrO levels are relatively insensitive.

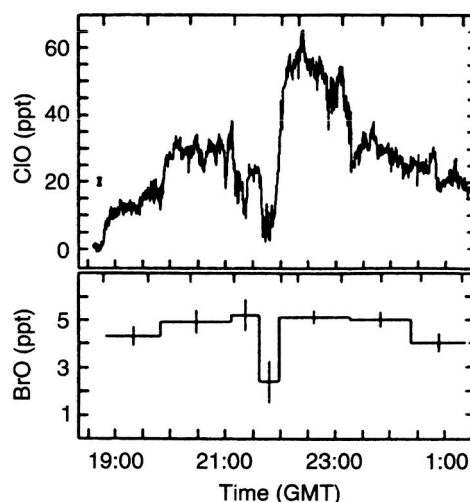


Figure 50: ClO and BrO measurements from the Harvard ClO/BrO instrument for the ER-2 flight of February 13, 1988. Vertical bars indicate abundances detectable with a signal-to-noise ratio of 2. Adapted from Brune *et al.* (1988).

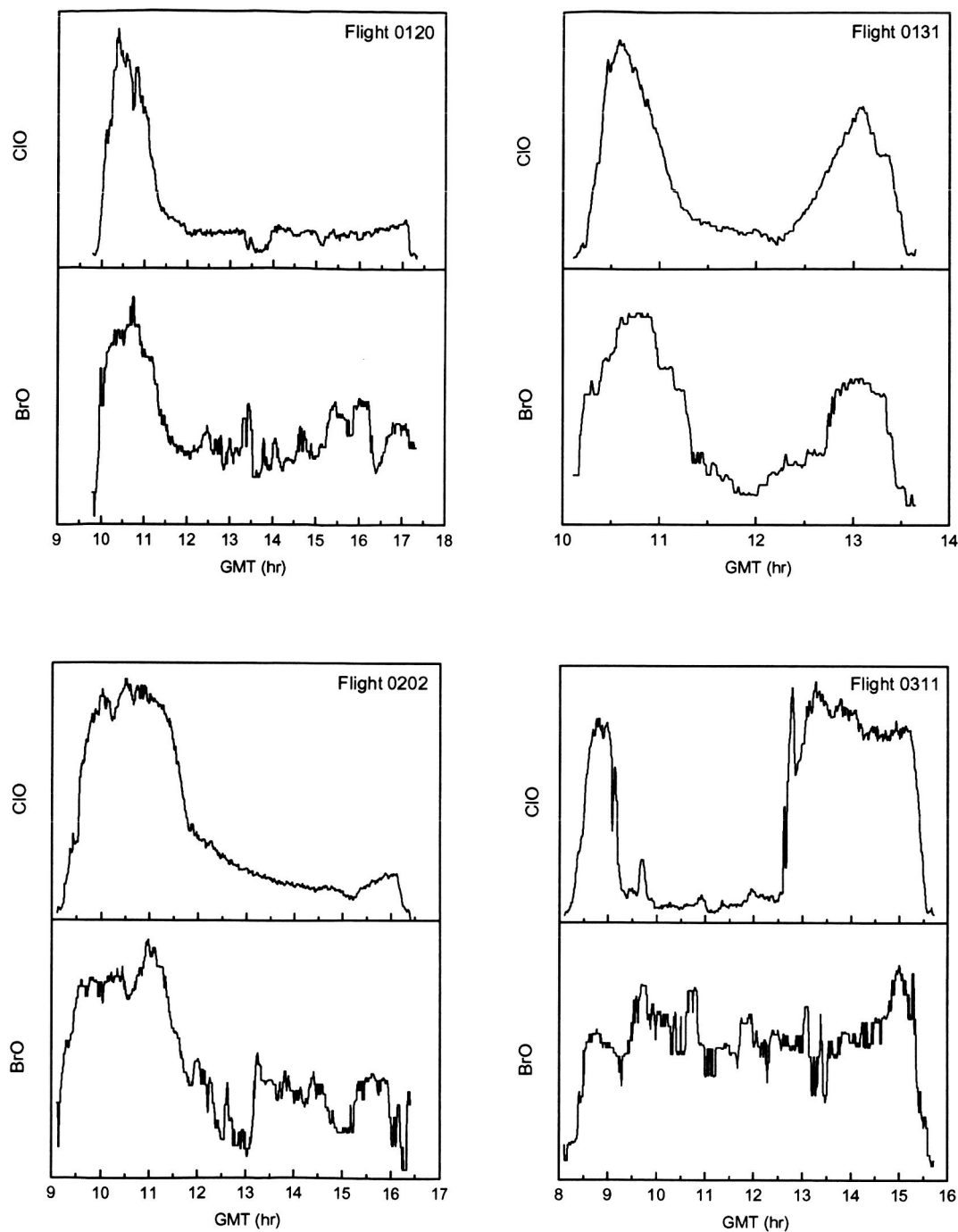


Figure 51: Observed ClO and BrO signals for selected flights of the SOLVE mission. The flights of 0120, 0131, and 0202 occurred completely within the Arctic vortex. The flight of 0311 began and ended in the vortex but was outside during the middle portion of the flight.

References

- Anderson, J. G, H. J. Grassl, R. E. Shetter, and J. J. Margitan, "Stratospheric free chlorine measured by balloon-borne *in situ* resonance fluorescence," *J. Geophys. Res.* **85**, 2869–87, 1980.
- Avallone, L. M., "In situ measurements of ClO and implications for the chemistry of inorganic chlorine in the lower stratosphere," PhD Thesis, Harvard University, 1993.

- Avallone, L. M., and D. W. Toohey, "Tests of halogen photochemistry using in situ measurements of ClO and BrO in the lower polar stratosphere," *J. Geophys. Res.* **106**, 10,411–21, 2001.
- Baer, S., H. Hippler, R. Rahn, M. Siefke, N. Seizinger, and J. Troe, "Thermodynamic and kinetic properties of the reaction $\text{Cl} + \text{O}_2 + \text{M} \leftrightarrow \text{ClOO} + \text{M}$ in the range 160–300 K and 1–1000 bar," *J. Chem. Phys.* **95**, 6463–70, 1991.
- Bloss, W. J., S. L. Nickolaisen, R. J. Salawitch, R. R. Friedl, and S. P. Sander, "Kinetics of the ClO self-reaction and 210 nm absorption cross section of the ClO dimer," *J. Phys. Chem. A* **105**, 11,226–39, 2001.
- Bloss, W. J., T. J. Gravestock, D. E. Heard, T. Ingham, G. P. Johnson, and J. D. Lee, "Application of a compact all solid-state laser system to the in situ detection of atmospheric OH, HO₂, NO and IO by laser-induced fluorescence," *J. Environ. Monit.* **5**, 21–8, 2003.
- Bonne, G. P., et al., "An examination of the inorganic chlorine budget in the lower stratosphere," *J. Geophys. Res.* **105**, 1957–71, 2000.
- Brune, W.H., D.W. Toohey, J.G. Anderson, W.L. Starr, J.F. Vedder, and E.F. Danielson, "In situ northern mid-latitude observations of ClO, O₃, and BrO in the wintertime lower stratosphere," *Science* **242**, 558–62, 1988.
- Brune, W. H., J. G. Anderson, and K. R. Chan, "In situ observations of ClO in the Antarctic: ER-2 aircraft results from 54°S to 72°S latitude," *J. Geophys. Res.* **94**, 16,649–63, 1989.
- Burkholder, J. B., J. J. Orlando, and C. J. Howard, "Ultraviolet absorption cross sections of Cl₂O₂ between 210 and 410 nm," *J. Phys. Chem.* **94**, 687–95, 1990.
- Cox, R. A. and G. D. Hayman, "The stability and photochemistry of dimers of the ClO radical and implications for Antarctic ozone depletion," *Nature* **332**, 796–800, 1988.
- Gerbig, C., J. C. Lin, S. C. Wofsy, B. C. Daube, A. E. Andrews, B. B. Stephens, P. S. Bakwin, and C. A. Grainger, "Constraining regional-to-continental-scale fluxes of CO₂ with atmospheric observations over a continent: A receptor-oriented analysis of COBRA data," submitted to *J. Geophys. Res.*, 2002.
- Hanisco, T. F., et al., "Quantifying the rate of heterogeneous processing in the Arctic polar vortex with in situ observations of OH," *J. Geophys. Res.* **107**(D20), 8278, doi:10.1029/2001JD000425, 2002.
- Hanisco, T. F., J. B. Smith, R. M. Stimpfle, D. M., Wilmouth, J. G. Anderson, E. C. Richard, and T. P. Bui, "In situ observations of HO₂ and OH obtained on the NASA ER-2 in the high ClO conditions of the 1999/2000 Arctic polar vortex," *J. Geophys. Res.* **107**(D20), 8283, doi:10.1029/2001JD001024, 2002.
- Hints, E. J., K. A. Boering, E. M. Weinstock, J. G. Anderson, B. L. Gary, L. Pfister, B. C. Daube, S. C. Wofsy, M. Loewenstein, J. R. Podolske, J. J. Margitan and T. P. Bui, "Troposphere-to-stratosphere transport in the lowermost stratosphere from measurements of H₂O, CO₂, N₂O and O₃," *Geophys. Res. Lett.* **25**(14), 2655–8, July 15, 1998.
- Huder, K. J. and W. B. DeMore, "Absorption cross sections of the ClO dimer," *J. Phys. Chem.* **99**, 3905–8, 1995.
- Liu, H.C., P. K. Wang, and R. E. Schlesinger, R.E., "A numerical study of cirrus clouds. Part II: Effects of ambient temperature, stability, radiation, ice microphysics and microdynamics on cirrus evolution," *J. Atmos. Sci.* **60**(9), 1097–19, 2003.
- Logan, J. A., I. A. Megretskaya, A. J. Miller, G. C. Tiao, D. Choi, L. Zhang, R. S. Stolarski, G. J. Labow, S. M. Hollandsworth, G. E. Bodeker, H. Claude, D. De Muer, J. B. Kerr, D. W. Tarasick, S. J. Oltmans, B. Johnson, F. Schmidlin, J. Staehelin, P. Viatte, and O. Uchino,

- "Trends in the vertical distribution of ozone: A comparison of two analyses of ozonesonde data," *J. Geophys. Res.* **104**, 26,373–99, 1999.
- Massie, S., A. Gettelman, W. Randel, and D. Baumgardner, "Distribution of tropical cirrus in relation to convection," *J. Geophys. Res.* **107**(D21), 4591, doi:10.1029/2001JD001293, 2002.
- Mauldin, R. L., J. B. Burkholder, and A. R. Ravishankara, "A photochemical, thermodynamic and kinetic study of ClOO," *J. Phys. Chem.* **96**, 2582–8, 1992.
- Newman, P. A., et al., "An overview of the SOLVE/THESEO 2000 campaign," *J. Geophys. Res.* **107**, 8259, doi:10.1029/2001JD001303, 2002.
- Nicholas, J. E., and R. G. W. Norrish, "Some reactions in the chlorine and oxygen system studies by flash photolysis," *Proc. Royal Soc. A* **307**, 391–7, 1968.
- Nicovich, J. M., K. D. Kreutter, C. J. Shackelford, and P. H. Wine, "Thermochemistry and kinetics of the Cl + O₂ association reaction," *Chem. Phys. Lett.* **179**, 367–73, 1991.
- Potter, B., and J. R. Holton, "The of monsoon convection in the dehydration of the lower tropical stratosphere," *J. Atmos. Sci.* **52**, 1034, 1995.
- Randall, C. E., et al., "Reconstruction of three-dimensional ozone fields using POAM III during SOLVE," *J. Geophys. Res.* **107**, SOL 42, 2002.
- Salawitch, R. J., et al., "Chemical loss of ozone in the Arctic polar vortex in the winter of 1991–1992," *Science* **261**, 1146–9, 1993.
- Salawitch, R. J., et al., "The distribution of hydrogen, nitrogen, and chlorine radicals in the lower stratosphere: Implications for changes in O₃ due to emission of NO_y from supersonic aircraft," *Geophys. Res. Lett.* **21**, 2547–50, 1994.
- Sander, S. P., et al., *Chemical Kinetics and Photochemical Data for Use in Stratospheric Modeling, Evaluation Number 13*, JPL Publ. 00-3, 2000.
- Sander, S. P., et al., *Chemical Kinetics and Photochemical Data for Use in Stratospheric Modeling, Evaluation Number 14*, JPL Publ. 02-25, 2002.
- Smith, J. B., E. Weinstock, J. V. Pittman, D. Sayres, and J. G. Anderson, "Observations and implications of supersaturation in the presence of cirrus in the tropical and subtropical upper troposphere," in preparation, 2005.
- Spackman, J. R., E. M. Weinstock, J. G. Anderson, C. R. Webster, and D. F. Hurst, "Deducing transport into the lowermost stratosphere from *in situ* measurements of water vapor, CH₄, and N₂O: Implications for mid-latitude ozone," in preparation, 2005.
- Stimpfle, R. M., D. M. Wilmouth, R. J. Salawitch, and J. G. Anderson, "The first measurements of ClOOCl in the stratosphere: The coupling of ClOOCl and ClO in the arctic polar vortex," *J. Geophys. Res.* **109**, D03301, doi:10.1029/2003JD003811, February 4, 2004.
- Trolier, M., R. L. Mauldin, and Ravishankara, A. R., "Rate coefficient for the termolecular channel of the self-reaction of ClO," *J. Phys. Chem.* **94**, 4896–4907, 1990.
- Twohy, C.H., C. F. Clement, and B. W. Gandrud, "Deep convection as a source of new particles in the midlatitude upper troposphere," *J. Geophys. Res.* **107**(D21), 4560, 2002.
- Wilmoth, D. M., "Laboratory studies and *in situ* stratospheric observations of inorganic chlorine and bromine species critical to catalytic ozone destruction," PhD Thesis, Harvard University, 2002.
- Wongdontri-Stupor, W., R. Simonaitis, and J. Heicklen, "The reaction of ClOO with NO," *Geophys. Res. Lett.* **5**, 1005–8, 1978.
- World Meteorological Organization, *Scientific Assessment of Ozone Depletion: 2002, Global Ozone Research and Monitoring Project–Report No. 47*, 498 pp., Geneva, 2003. Available at <http://www.wmo.ch/web/arep/ozone/html> and <http://www.unep.org/ozone/sap2002.shtml>.

Yin, Y., K. Carslaw, and D. Parker, "Redistribution of trace gases by convective clouds—mixed phase processes," *Atmos. Chem. Phys.* **2**, 293–306, 2002.

Publications resulting from this funding:

Moyer, E. J., D. B. Kirk-Davidoff, E. Weinstock, J. B. Smith, J. V. Pittman, and J. G. Anderson, "In-situ observations of the control of water vapor in the tropical upper troposphere and stratosphere," in preparation, 2005.

Sayres, D. S., J. V. Pittman, J. B. Smith, E. M. Weinstock, J. G. Anderson, G. Heymsfield, L. Li, A. Fridlind, and A. S. Ackerman, Methods for validation and intercomparison of remote sensing and *in situ* ice water measurements: Case studies from CRYSTAL-FACE and Model Results, *J. Geophys. Res.*, in preparation, 2005.

Smith, J. B., E. Weinstock, J. V. Pittman, D. Sayres, and J. G. Anderson, "Observations and implications of supersaturation in the presence of cirrus in the tropical and subtropical upper troposphere," in preparation, 2005.

Spackman, J. R., E. M. Weinstock, J. G. Anderson, C. R. Webster, and D. F. Hurst, "Deducing transport into the lowermost stratosphere from *in situ* measurements of water vapor, CH₄, and N₂O: Implications for mid-latitude ozone," in preparation, 2005.

Stimpfle, R. M., D. M. Wilmouth, R. J. Salawitch, and J. G. Anderson, The first measurements of ClOOCl in the stratosphere: The coupling of ClOOCl and ClO in the arctic polar vortex, *J. Geophys. Res.* **109**, D03301, doi:10.1029/2003JD003811, February 4, 2004.

Weinstock, E. M., E. J. Hintsa, D. B. Kirk-Davidoff, J. G. Anderson, A. E. Andrews, R. L. Herman, C. R. Webster, M. Loewenstein, J. R. Podolske and T. P. Bui, "Constraints on the seasonal cycle of stratospheric water vapor using *in situ* measurements from the ER-2 and a CO photochemical clock," *J. Geophys. Res.* **106**(D19), 22,707–24, 2001.

Weinstock, E. M., J. B. Smith, D. Sayres, J. R. Spackman, J. V. Pittman, N. Allen, J. Demusz, M. Greenberg, M. Rivero, L. Solomon and J. G. Anderson, "Measurements of the total water content of cirrus clouds: Instrument details and calibration," *J. Atmos. and Oceanic Techn.*, submitted 2005.

Weinstock, E. M., J. B. Smith, D. Sayres, J. V. Pittman, N. Allen and J. G. Anderson, "Measurements of the total water content of cirrus clouds: Instrument performance and validation," *J. Atmos. and Oceanic Techn.*, submitted 2005.

There are no inventions resulting from this funding.